

Resonance Phenomena in a Scalar Delay Differential Equation with Two State-Dependent Delays*

R. C. Calleja[†], A. R. Humphries[‡], and B. Krauskopf[§]

Abstract. We study a scalar delay differential equation (DDE) with two delayed feedback terms that depend linearly on the state. The associated constant-delay DDE, obtained by freezing the state dependence, is linear and without recurrent dynamics. With state-dependent delay terms, on the other hand, the DDE shows very complicated dynamics. To investigate this, we perform a bifurcation analysis of the system and present its bifurcation diagram in the plane of the two feedback strengths. It is organized by Hopf-Hopf bifurcation points that give rise to curves of torus bifurcation and associated two-frequency dynamics in the form of invariant tori and resonance tongues. We numerically determine the type of the Hopf-Hopf bifurcation points by computing the normal form on the center manifold; this requires the expansion of the functional defining the state-dependent DDE in a power series whose terms up to order three contain only constant delays. We implemented this expansion and the computation of the normal form coefficients in MATLAB using symbolic differentiation, and the resulting code `HHnfDDEsd` is supplied as a supplement to this article. Numerical continuation of the torus bifurcation curves confirms the correctness of our normal form calculations. Moreover, it enables us to compute the curves of torus bifurcations more globally and to find associated curves of saddle-node bifurcations of periodic orbits that bound the resonance tongues. The tori themselves are computed and visualized in a three-dimensional projection, as well as the planar trace of a suitable Poincaré section. In particular, we compute periodic orbits on locked tori and their associated unstable manifolds (when there is a single unstable Floquet multiplier). This allows us to study transitions through resonance tongues and the breakup of a 1:4 locked torus. The work presented here demonstrates that state dependence alone is capable of generating a wealth of dynamical phenomena.

Key words. state-dependent delay differential equations, bifurcation analysis, invariant tori, resonance tongues, Hopf-Hopf bifurcation, normal form computation

AMS subject classifications. 34K60, 34K18, 37G05, 37M20

DOI. 10.1137/16M1087655

1. Introduction. Time delays arise naturally in numerous areas of application as an unavoidable phenomenon, for example, in balancing and control [8, 19, 35, 39, 64, 65, 66, 67],

*Received by the editors August 4, 2016; accepted for publication (in revised form) by J. Sieber May 1, 2017; published electronically August 17, 2017.

<http://www.siam.org/journals/siads/16-3/M108765.html>

Funding: The first author's work was supported by the NSERC and the Centre de Recherches Mathématiques. The second author's work was supported by the National Science and Engineering Research Council (NSERC), Canada, through the Discovery Grant program.

[†]Depto. Matemáticas y Mecánica, IIMAS, Universidad Nacional Autónoma de México, 01000 México (calleja@mym.iimas.unam.mx).

[‡]Departments of Mathematics & Statistics, and, Physiology, McGill University, Montreal, Quebec H3A 0B9, Canada (Tony.Humphries@mcgill.ca).

[§]Department of Mathematics, University of Auckland, Auckland 1142, New Zealand (b.krauskopf@auckland.ac.nz).

machining [36], laser physics [40, 46, 54], agent dynamics [52, 53, 70, 73], neuroscience and biology [1, 18, 20, 42, 79], and climate modeling [13, 41, 48]. Important sources of delays are communication times between components of a system, maturation and reaction times, and the processing time of information received. When they are sufficiently large compared to the relevant internal time scales of the system under consideration, then the delays must be incorporated into its mathematical description. This leads to mathematical models in the form of delay differential equations (DDEs). In many situations the relevant delays can be considered to be fixed; examples are the travel time of light between components of a laser system, and machining with rotating tools.

There is a well established theory of DDEs with a finite number of constant delays as infinite-dimensional dynamical systems; see, for example, [6, 26, 27, 12, 74, 75]. Usually the phase space of the dynamical system is taken to be $C = C([-τ, 0], \mathbb{R}^d)$, the Banach space of continuous functions mapping $[-τ, 0]$ to \mathbb{R}^d , where d is the number of variables and $τ$ is the largest of the delays. The DDE can then be written as a retarded functional differential equation,

$$(1.1) \quad u'(t) = F(u_t),$$

where $F : C \rightarrow \mathbb{R}^d$ and where $u_t \in C$ for each $t \geq 0$ is the function

$$(1.2) \quad u_t(\theta) = u(t + \theta), \quad \theta \in [-\tau, 0].$$

In other words, an initial condition consists of a function over the time interval from the (maximal) delay τ ago up to time 0, which (under appropriate mild assumptions) determines the solution for all times $t > 0$. In fact, solutions of constant-delay DDEs depend smoothly on their initial conditions, and linearizations at equilibria and periodic solutions have at most finitely many unstable eigendirections. As a consequence, bifurcation theory for this class of DDEs is analogous to that for ordinary differential equations (ODEs), and one finds the same types of bifurcations. In particular, center manifold and normal form methods allow for the local reduction of the DDE to an ODE describing the dynamics near a bifurcation point of interest. Moreover, advanced numerical tools for simulation and bifurcation analysis of DDEs with constant delays have become available in recent years [4, 5, 7, 17, 47, 72, 77]. These theoretical and numerical tools have been applied very successfully in many application areas, including those mentioned above.

It is very important to realize that treating the delays that arise as constant is a modeling assumption that must be justified. This can be argued successfully, for example, in machining when the tool has nearly infinite stiffness perpendicular to the cutting direction [75], or in laser dynamics where light travels over a fixed distance [40]. On the other hand, in many contexts, including in biological systems and in control problems [9, 10, 11, 21, 36, 38, 68, 82], the delays one encounters are not actually constant. In particular, they may depend on the state in a significant way, that is, change dynamically during the time-evolution of the system.

DDEs with state-dependent delays have been an active area of research in recent years. Many parts of the general theory of DDEs with constant delays have been extended to also cover state-dependent DDEs, where τ is now a global bound on the maximal possible delay; see [29] and the discussion in [34]. However, the mathematical theory is considerably

more complicated and as yet incomplete. Solutions of state-dependent DDEs do not depend smoothly on initial conditions or parameters unless extra assumptions are made on the initial conditions [28], and this dramatically complicates arguments around key concepts, requiring new theory and proofs for asymptotics, the initial value problem, bifurcations, and invariant manifolds. Indeed, these important elements of the theory have been addressed only recently [29, 32, 49, 59, 60, 71, 80, 81]. Similarly, the numerical bifurcation analysis of state-dependent DDEs is more involved. Recent developments include approaches for the continuation of solutions and bifurcations for state-dependent delay equations [34, 72]. The paper [47] has methods for finding invariant manifolds for DDEs with constant delays. Issues that remain outstanding include smoothness of center manifolds and, therefore, also normal form reductions.

In light of the considerable additional difficulty, state-dependent delays are quite often replaced by constant delays—by considering some sort of average or nominal delays—even in modeling situations when this cannot be readily justified. The obvious question is whether and when a state-dependent DDE displays dynamics that is considerably different from that of the associated constant-delay DDE.

In this paper we address this practical question by studying a prototypical DDE with state-dependent delays, rather than an equation arising from a specific application. This example DDE has the important property that it exhibits very complicated dynamics with state dependence, while it reduces to a linear DDE with only trivial dynamics if the delays are made constant. Specifically, we consider here the scalar DDE

$$(1.3) \quad u'(t) = -\gamma u(t) - \kappa_1 u(\alpha_1(t, u(t))) - \kappa_2 u(\alpha_2(t, u(t))), \quad \text{where } \alpha_i(t, u(t)) = t - a_i - c_i u(t).$$

The two delay terms, with feedback strengths $\kappa_1, \kappa_2 \geq 0$, are given by the linear functions $\alpha_i(t, u(t))$, where a_i and c_i are strictly positive. In the absence of the delay terms, that is, for $\kappa_1 = \kappa_2 = 0$, (1.3) is a linear scalar equation whose solutions decay exponentially to the origin with rate $\gamma > 0$. For $\kappa_1, \kappa_2 \neq 0$, on the other hand, the delay terms are present and constitute a feedback. When $c_1 = c_2 = 0$ the DDE (1.3) is linear with two fixed delays a_1 and a_2 , while for $c_1, c_2 \neq 0$ the delay terms are linearly state-dependent.

A singularly perturbed version of (1.3) is studied in [33, 43, 61]. In [43] solutions are considered near the singular Hopf bifurcations, while [33] constructs large amplitude singular solutions and studies the singular limit of the fold bifurcations. Equation (1.3) is a generalization of the corresponding single delay DDE which can be obtained from (1.3) by setting $\kappa_2 = 0$. The single delay DDE was first introduced in a singularly perturbed form as an example problem by Mallet-Paret and Nussbaum in [60] and considered extensively in [62] as part of a series of papers [56, 57, 58, 60, 61, 62] studying singularly perturbed solutions of state-dependent DDEs.

We consider (1.3) with all parameters nonnegative, and without loss of generality assume that $a_2 > a_1$. We also assume

$$(1.4) \quad \gamma > \kappa_2.$$

It is shown in [34] that if (1.4) holds and

$$(1.5) \quad \phi(t) \in \left(-\frac{a_1}{c}, \frac{a_1}{\gamma c} (\kappa_1 + \kappa_2) \right) \quad \forall t \in \left[-a_2 - \frac{a_1}{\gamma} (\kappa_1 + \kappa_2), 0 \right],$$

then (1.3) is well posed and all solutions of the initial value problem composed of solving (1.3) for $t \geq 0$ with the initial function

$$(1.6) \quad u(t) = \phi(t), \quad t \leq 0,$$

satisfy

$$(1.7) \quad u(t) \in \left(-\frac{a_1}{c}, \frac{a_1}{\gamma c}(\kappa_1 + \kappa_2) \right) \quad \forall t > 0.$$

This bound on the solution also implies a bound on the delays, with (1.3) and (1.7) implying that

$$(1.8) \quad \alpha_i(t, u(t)) \in \left(t - a_i - \frac{a_1}{\gamma}(\kappa_1 + \kappa_2), t \right) \subset \left(t - a_2 - \frac{a_1}{\gamma}(\kappa_1 + \kappa_2), t \right) \quad \forall t \geq 0$$

and, in particular, the state-dependent delays can never become advanced when $\gamma > \kappa_2$. It is also shown in [34] that there exists $\xi \in [0, a_2 + \frac{a_1}{\gamma}(\kappa_1 + \kappa_2)]$ such that $\alpha_i(t, u(t))$ is a strictly monotonic increasing function of t for $t > \xi$.

Notice that the DDE (1.3) is of the form (1.1) with $d = 1$ if we let

$$(1.9) \quad F(\phi) = -\gamma\phi(0) - \kappa_1\phi(-a_1 - c\phi(0)) - \kappa_2\phi(-a_2 - c\phi(0)).$$

We take $\tau = a_2 + \frac{a_1}{\gamma}(\kappa_1 + \kappa_2)$, which by (1.8) ensures that $\alpha_i(t, u(t)) \in [t - \tau, t]$ for $t \geq 0$ and the function u_t includes all the information necessary to evaluate $u'(t)$. Moreover, provided the initial function ϕ is Lipschitz, it follows from standard DDE theory [14] that the initial value problem has a unique solution satisfying (1.7).

For $c_1 = c_2 = 0$ general theory [6, 26, 27] states that, depending on the values of γ , κ_1 , and κ_2 , all trajectories of (1.3) decay to the origin or grow exponentially in time. In other words, the dynamics of the system without state dependence in the delay terms is indeed trivial. On the other hand, it was shown in [34] that state dependence of the delay terms changes the dynamics completely, since the function F in (1.9) is nonlinear. Therefore, the state dependence of the delays for $c_1, c_2 \neq 0$ is responsible for nonlinearity in the system. The two delay terms introduce two oscillatory degrees of freedom into the system, which may then interact nonlinearly. As a result, the dynamics of the DDE (1.3) is no longer linear; rather it is, colloquially speaking, potentially at least as complicated as that of two coupled nonlinear oscillators with dissipation. Indeed, the interest in (1.3) arises from the fact that it is effectively the simplest example one can consider of a DDE with several state-dependent delays. In particular, any nontrivial dynamics that one finds must be due to the state dependence.

Throughout this paper we will take

$$(1.10) \quad \gamma = 4.75, \quad a_1 = 1.3, \quad a_2 = 6, \quad c_1 = c_2 = 1,$$

and vary the values of (κ_1, κ_2) with $\kappa_2 \in (0, 4.75)$ to satisfy (1.4). The parameter set (1.10) was first identified as producing interesting dynamics for (1.3) in [34]. There, one-parameter bifurcation diagrams for (1.3) were produced for this parameter set with fixed values of κ_2 . In

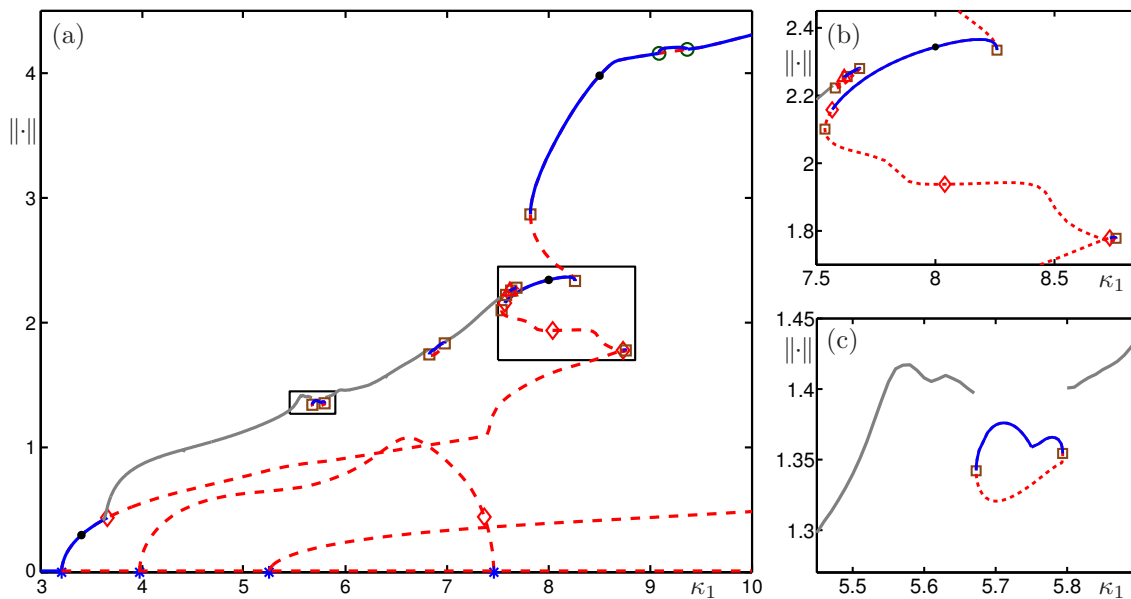


Figure 1. One-parameter bifurcation diagram in κ_1 of (1.3), showing the norm $\|u(t)\| = \max u(t) - \min u(t)$ of periodic orbits bifurcating from Hopf bifurcations of the trivial solution (a). Stable orbits are shown as solid blue curves and unstable ones as dashed red curves; indicated are points of Hopf bifurcation (stars), saddle-node of limit cycle bifurcation (squares), period-doubling bifurcations (circles) and torus bifurcation (diamonds). Also shown is a grey curve of tori that bifurcate from the principal branch of periodic orbits at $\kappa_1 \approx 3.6557$. Panels (b) and (c) are two enlargements respectively near the stable part of the principal branch and near an isola of periodic orbits associated with 1:4 phase locking. The black dots correspond to the stable periodic orbits shown in Figure 2. Here $\kappa_2 = 3.0$ and, throughout, $\gamma = 4.75$, $a_1 = 1.3$, $a_2 = 6.0$, and $c_1 = c_2 = 1.0$. Reproduced with permission from [34]. [Copyright 2012, American Institute of Mathematical Sciences.]

[34], it was also noticed that the bifurcation diagram is topologically very different for other choices of parameters.

Figure 1 illustrates the results obtained in [34] with $\kappa_2 = 3$ and the other parameters given by (1.10), where the dynamics of (1.3) was explored by means of finding the Hopf bifurcations of the zero solution and continuing the branches of bifurcating periodic orbits. As panel (a) shows, the zero solution loses stability in a first Hopf bifurcation at $\kappa_1 \approx 3.2061$ where a branch of stable periodic solutions emerges. These lose stability in a torus (or Neimark–Sacker) bifurcation at $\kappa_1 \approx 3.6557$. The branch of (unstable) saddle periodic solutions regains stability in the interval $\kappa_1 \in [7.5665, 8.2585]$ after two saddle-node (or fold) bifurcations and several further torus bifurcations; see the enlargement in Figure 1(b). A further two saddle-node bifurcations lead to a hysteresis loop of the branch, and the periodic solution is stable again for $\kappa_1 > 7.82$, except for $\kappa_1 \in [9.0857, 9.3624]$, where a pair of period-doubling bifurcations lead to a short interval of stable period-doubled solutions. Also shown in Figure 1(a) are branches of bifurcating stable tori, which are represented by the maximum of the norm along a numerically computed trajectory of sufficient length. As is expected from general theory, one finds locked dynamics on the torus when κ_1 passes through resonance tongues. The associated periodic orbits on the torus can be continued, and Figure 1(c) shows the isola of

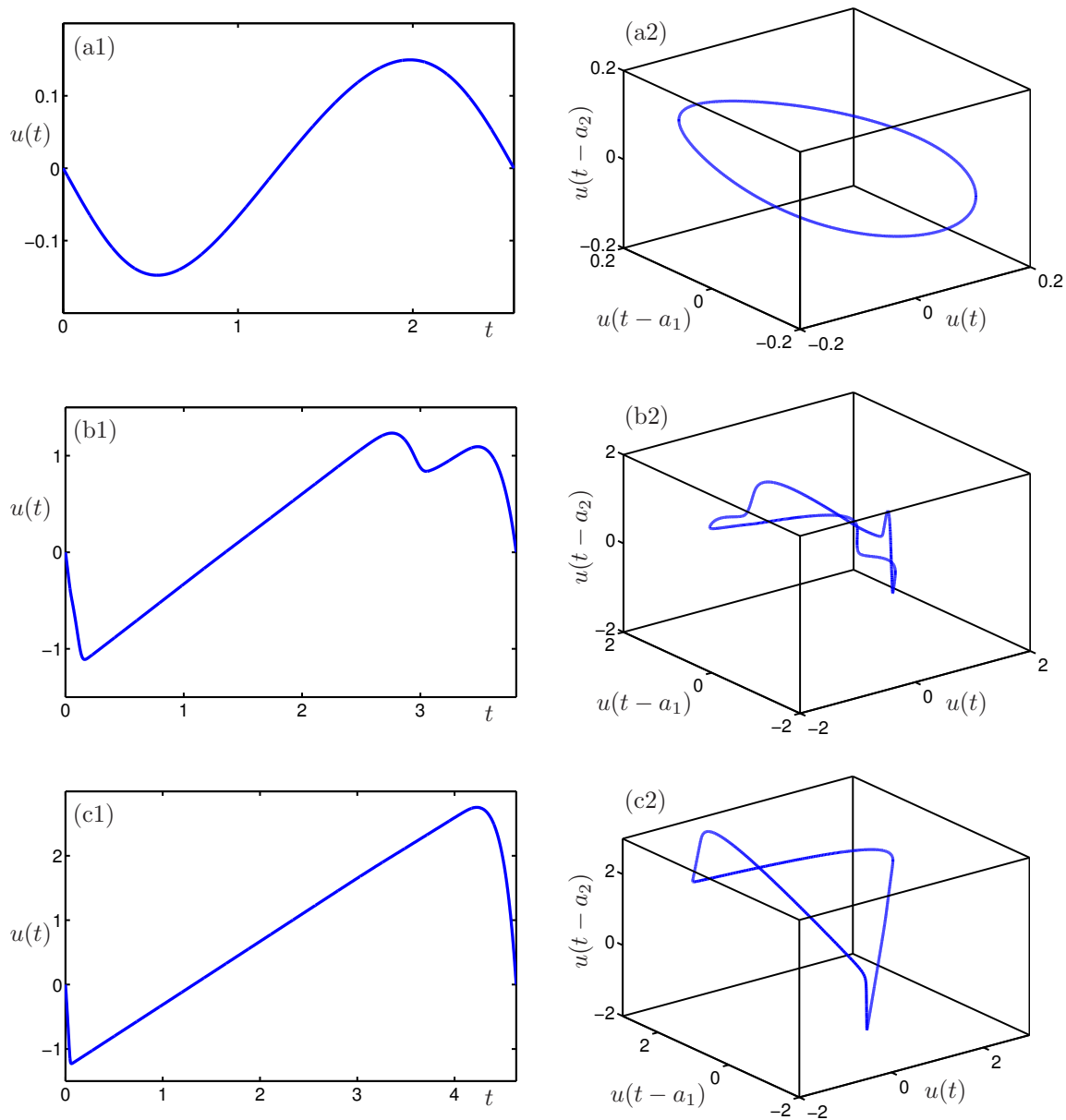


Figure 2. Three stable periodic orbits from the principal branch in Figure 1, shown as a time series over one period (left column) and in projection into $(u(t), u(t - a_1), u(t - a_2))$ -space (right column); here $\kappa_1 = 3.4$ in row (a), $\kappa_1 = 8.0$ in row (b), and $\kappa_1 = 8.5$ in row (c).

periodic solutions corresponding to 1 : 4 phase locking. Notice that there are further Hopf bifurcation points and bifurcating branches of periodic solutions in Figure 1(a), but none of them are stable.

Figure 2 shows examples of stable periodic solutions from the three main ranges of stability discussed above, for values of κ_1 as indicated by the black dots in Figure 1(a). Shown in

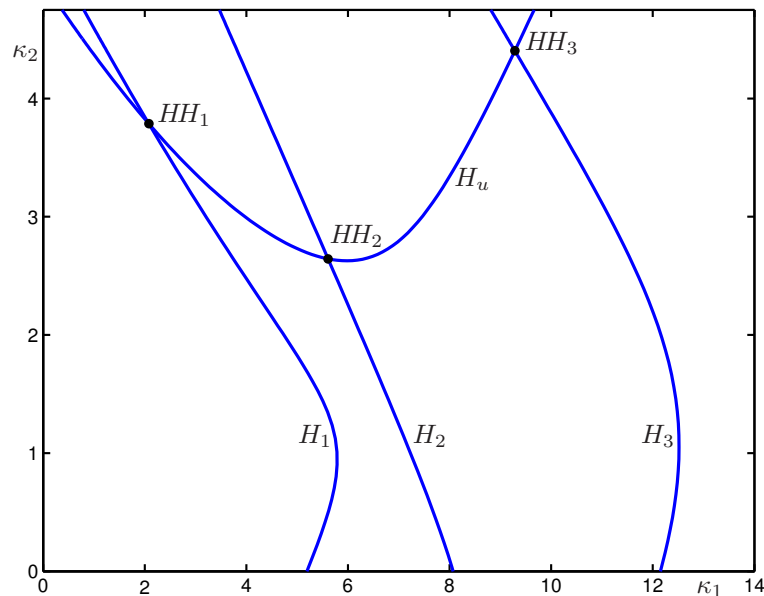


Figure 3. Curves of Hopf bifurcation in the (κ_1, κ_2) -plane of (1.3); the upper Hopf bifurcation curve H_u intersects the Hopf bifurcation curves H_j for $j = 1, 2, 3$ at Hopf-Hopf bifurcation points HH_j .

Figure 2 are the time series of $u(t)$ over one period and the orbit in projection onto $(u(t), u(t - a_1)u(t - a_2))$ -space of the respective periodic solution. The periodic solution in row (a) of Figure 2 is almost perfectly sinusoidal, as is expected immediately after a Hopf bifurcation. The periodic solution in row (b), on the other hand, features two local maxima and is close to a saw-tooth shape. Similarly, the periodic solution in Figure 2(c) is very close to a simple saw-tooth, with a single linear rise and then a sharp drop in $u(t)$. Sawtooth periodic solutions and some of their bifurcations are considered in [33], where a singularly perturbed version of (1.3) is studied.

The results from [34], summarized in Figures 1 and 2, clearly show that (1.3) features highly nontrivial dynamics due to the state dependence. On the other hand, a more detailed bifurcation analysis of the system has not been performed. The only two-parameter continuation performed in [34] is limited to that of the curves of Hopf bifurcations in the (κ_1, κ_2) -plane. It identified Hopf-Hopf (or double Hopf) bifurcations, but neither they nor the curves of torus bifurcations emerging from them were investigated in that work. Moreover, the bifurcating tori were not studied in detail in [34]; in particular, stable tori themselves were not computed when phase locked.

To highlight the full extent of the dynamics generated by the state dependence, in this work we present a bifurcation study of (1.3) that goes well beyond that in [34]. Our focus is on two-frequency dynamics and associated resonance phenomena; our main objects of study are the bifurcation diagram in the (κ_1, κ_2) -plane and the associated dynamics in phase space. The starting point of our investigation is the arrangement of the Hopf bifurcation curves of (1.3) shown in Figure 3.

A Hopf bifurcation occurs when a complex conjugate pair of characteristic values crosses

the imaginary axis in the linearized system. State-dependent DDEs are linearized around equilibria by first freezing the state-dependent delays at their steady-state values. This technique has long been applied heuristically, but more recently has been established rigorously by Györi and Hartung [24, 25] for a class of problems including (1.3). Hence, we obtain

$$(1.11) \quad u'(t) = -\gamma u(t) - \kappa_1 u(t - a_1) - \kappa_2 u(t - a_2)$$

as the linearization of (1.3) about the trivial steady state $u \equiv 0$. The characteristic equation for (1.11) is given by

$$(1.12) \quad 0 = \lambda + \gamma + \kappa_1 e^{-a_1 \lambda} + \kappa_2 e^{-a_2 \lambda},$$

and so at a Hopf bifurcation we have $\lambda = \pm i\omega$ with

$$(1.13) \quad 0 = i\omega + \gamma + \kappa_1 e^{-ia_1 \omega} + \kappa_2 e^{-ia_2 \omega}.$$

The three curves $H_1, H_2,$ and H_3 in Figure 3 emerge from $\kappa_2 = 0$ and are functions of κ_2 . These three Hopf bifurcation curves are intersected by the curve H_u , which exists only above $\kappa_2 \approx 2.627$ and is a function of κ_1 . The three intersection points $HH_1, HH_2,$ and HH_3 are codimension-two points of the Hopf-Hopf bifurcation. From (1.13) it follows that there are in fact infinitely many Hopf bifurcation curves of (1.3) as $\kappa_1 \rightarrow \infty$ and, consequently, other Hopf-Hopf points; however, these are not shown in Figure 3 because we concentrate here on the κ_1 -range of $[0, 14]$. Note that we show the (κ_1, κ_2) -plane only for $\kappa_2 \leq \gamma = 4.75$, because this is the κ_2 -range for which we know that the state-dependent DDE is well posed.

The numerical computation of Hopf bifurcations in state-dependent DDEs has been implemented in the DDE-BIFTOOL software package [17, 72], and this capability actually predates their rigorous proof. Eichmann [16] was the first to establish a rigorous Hopf bifurcation theorem for state-dependent DDEs, but results have appeared in the published literature only much more recently [32, 71]. We perform here a calculation of the four-dimensional normal form ODE on the center manifold of the Hopf-Hopf points $HH_1, HH_2,$ and HH_3 . As far as we are aware, this is the first such calculation to determine the type of Hopf-Hopf bifurcations in a state-dependent DDE. The Hopf-Hopf normal form ODE with the multitude of cases that can arise in the unfolding is presented in detail in [51]. In constant-delay equations it has already been studied—see, for instance, [3]; the normal form procedure is also elaborated in [23] and has been implemented recently [78] as part of DDE-BIFTOOL [72] for constant delays only. Our approach is to derive a constant-delay DDE from the state-dependent DDE (1.3) by expanding the state dependence to sufficient order in (many) constant delays. The Hopf-Hopf normal form ODE can then be computed from this constant-delay DDE with established methods, and specifically we implemented the approach from [23]. In this way, we are able to determine the type of the Hopf-Hopf bifurcation and show that a pair of torus bifurcation curves emerges from each of the points $HH_1, HH_2,$ and HH_3 . The reduction to the constant-delay DDE and the corresponding resulting normal form coefficients are presented in section 2, where we also compare our results with those obtained from the DDE-BIFTOOL implementation. Further details of the normal form calculations can be found in M108765_01.pdf [local/web 322KB]. Our MATLAB code `HHnfDDEsd`, which implements the constant-delay expansion and computes the normal form coefficients for the Hopf-Hopf bifurcation, is available

as a supplement to this paper (see M108765_02.zip [local/web 6.79KB] and M108765_03.zip [local/web 14.5KB]).

The dynamics on the bifurcating tori may be quasi-periodic or locked, and this is organized by resonance tongues that are bounded by curves of saddle-node (or fold) bifurcations of periodic orbits. We proceed in section 3 by computing and presenting bifurcating stable quasi-periodic and phase-locked tori. The MATLAB [63] state-dependent DDE solver `ddesd` is used to find trajectories on stable invariant tori. In this way, we find quasi-periodic (or high-period) tori. To obtain locked tori, we find and continue the locked periodic solutions with the software package DDE-BIFTOOL [17, 72]. The unstable manifolds of the saddle periodic orbits on the torus are then represented as two-dimensional surfaces obtained by numerical integration of trajectories in these manifolds.

Since (1.3) is a scalar DDE, but its phase-space is infinite-dimensional, we consider finite-dimensional projections of the infinite-dimensional phase space. Moreover, we also show the tori in suitable projections of the Poincaré map defined by $u(t)$ passing through 0. This allows us to reveal the inherently low-dimensional character of these invariant tori and associated bifurcations.

We then perform in section 3.1 a bifurcation study of the emergence of tori and associated resonance phenomena. Specifically, we compute and illustrate in the (κ_1, κ_2) -plane the curves of torus bifurcation emerging from the Hopf-Hopf bifurcation point HH_1 and the associated structure of resonance tongues. We also consider in detail the properties and bifurcations of the invariant tori inside and near the regions of strong 1 : 3 and 1 : 4 resonances. More specifically, in section 3.2 we show how the 1 : 4 locked torus loses normal hyperbolicity and then breaks up in a complicated sequence of bifurcations as κ_1 is changed. Finally, in section 4 we present the overall bifurcation diagram in the (κ_1, κ_2) -plane, provide some conclusions, and point out directions for future research.

2. Normal form at Hopf-Hopf bifurcation. Here we derive the normal form of the Hopf-Hopf bifurcations of (1.3). For constant-delay DDEs a center manifold reduction [3, 23] transforms the DDE into an ODE on the center manifold, and the normal form of the Hopf-Hopf bifurcation for ODEs is well known and can be found in [51]. For state-dependent DDEs, the existence of a C^1 center-unstable manifold has been proved by several authors (for instance, see [50, 69, 76]), with verifiable regularity conditions that (1.3) satisfies, when the spectrum of (1.11) has eigenvalues λ satisfying that $\text{Re}(\lambda) \geq 0$. However, the existence of a C^3 regular center-unstable manifold, as required for the Hopf-Hopf bifurcation analysis, has not been rigorously established in the state-dependent case. Nor has the normal form of the Hopf-Hopf bifurcation for a state-dependent DDE previously been elaborated.

Noting that linearization of (1.3) reduces it to the constant-delay DDE (1.11), our approach is instead to obtain a series expansion of the right-hand side of (1.3) in which the low-order terms only involve constant delays. In particular, the state dependence will only appear in the higher-order remainder term. The derivation of the terms up to order three of the normal form DDE with constant delays near the Hopf-Hopf bifurcation is exact. We then, as is usual in the field, disregard the remainder term and consider only this truncated expansion. We conjecture that the truncated constant-delay DDE fully describes all of the dynamics near the Hopf-Hopf bifurcation in the state-dependent DDE. We then proceed by

applying the established center manifold reduction of [3, 23] to obtain an ODE on the center manifold. The flow restricted to the center manifold satisfies an ODE in four-dimensional space, which can be reduced to a normal form to determine the type of Hopf-Hopf bifurcation that occurs. The virtue of this method is that we study a four-dimensional ODE as opposed to an infinite-dimensional semiflow. Of course, this construction only works close to the point of the Hopf-Hopf bifurcation in parameter space, where the center manifold persists since the rest of the eigenvalues are at a positive distance from the imaginary axis; the center manifold should be a normally hyperbolic invariant manifold in the infinite-dimensional phase space.

Since the state dependence of the delays is the only source of nonlinearity in the DDE (1.3), the correct treatment of these state-dependent delays is essential to our results. Specifically, our strategy is as follows. We Taylor expand the state-dependent terms $u(t - a_i - cu(t))$ in time about their constant-delay reductions $u(t - a_i)$. This removes the state dependence from the equations, but at the cost of introducing derivatives of $u(t - a_i)$ in higher-order terms. Not wanting to deal with neutral DDEs, we remove the derivatives $\frac{d^k}{dt^k}u(t - a_i)$ by differentiating (1.3) $k - 1$ times and evaluating the resulting expression at $t - a_i$. This introduces additional delays into the DDE and also reintroduces the state dependence of the delays, but only in the quadratic and higher-order terms. The quadratic state-dependent delays are removed by the same process of Taylor expansion and substitution. We can repeat this process as many times as desired to obtain a DDE with only constant delays in the terms up to k th order for any k . Normal form theory for Hopf-Hopf bifurcation requires the expansion up to order three, which is why we stop at this order. By using the integral form of the remainder in Taylor's theorem, it is possible to obtain an explicit expression for the higher-order terms. In the current work, we conjecture, but do not prove, that the remainder term can indeed be disregarded. This allows us to apply the techniques of [3, 23] to the lower-order constant-delay part of our expanded DDE to determine the normal form equations, as well as the Hopf-Hopf unfolding bifurcation types.

There is a long and often inglorious history of Taylor expanding in DDEs to alter or eliminate the delay terms. It is obviously invalid to expand $u(t - a)$ about $u(t)$ when $|u(t - a) - u(t)|$ is large, which will be the typical case when a is not small. But related to the phenomenon of delay induced instability, even when u is close to steady state so that $|u(t - a) - u(t)| \ll 1$, expanding $u(t - a)$ about $u(t)$ can change the stability of the steady state; see [15] for examples. In the current work, we expand terms of the form $u(t - a - cu(t))$ about $u(t - a)$ close to steady state. Hence, not only is the difference in the u -values small, that is $|u(t - a - cu(t)) - u(t - a)| \ll 1$, but crucially the difference in the time values is also small, that is, $|(t - a - cu(t)) - (t - a)| = |cu(t)| \ll 1$.

Having found the normal form of the Hopf-Hopf bifurcation of (2.14), we compare the resulting bifurcations predicted by the normal form calculation with the numerically determined bifurcation curves for the full state-dependent DDE (1.3). Close to the Hopf-Hopf points we find very good agreement, which gives us confidence in the results obtained by both approaches. In particular, these results constitute strong numerical evidence that the resulting normal form for the expanded constant-delay DDE (2.14) is indeed that for the state-dependent DDE (1.3). While proving this conjecture is beyond the scope of this paper, we remark that such a proof, and indeed the expansions that we perform, require at least

C^3 regularity of (the solutions in) the manifold. To our knowledge, the best regularity result for the center manifolds in state-dependent DDEs establishes just C^1 regularity [50], and C^r regularity with $r > 1$ has not yet been established for center manifolds of state-dependent DDEs. Nevertheless, the expansions we perform here do not seem to present any obstruction to obtaining the formal expressions for small amplitudes of the function u . In fact, one notices that knowing the C^1 -smoothness of the local center-unstable manifold justifies that the solutions can be continued for negative times. Since in our case we are close to the steady state $u(t) = 0$, the delays are bounded and the solutions must be C^k smooth in time. Indeed, having C^k -regular solutions could lead to obtaining C^k -smooth time-1 maps, and these are perhaps the basis for constructing a C^k -smooth center manifold. This possible route to C^k regularity is already proposed in [29]. We also mention that results for invariant tori of state-dependent DDEs have been derived recently in spaces of smooth and analytic functions; see [30, 31].

We elaborate our steps as follows. In section 2.1, we present the details of the expansion of the state-dependent DDE to obtain a DDE with only constant delays up to order three. In section 2.2, we describe aspects of the projection onto the center manifold for this constant-delay DDE and present the derivation of the normal form coefficients. The algebraic details of these calculations are contained in supplemental file M108765_01.pdf [local/web 322KB]. In section 2.3 we use the normal form obtained to determine the type of the Hopf-Hopf bifurcation for the three Hopf-Hopf bifurcations seen in Figure 3.

2.1. Expansion of the nonlinearity. In this section, we perform the expansion of the state-dependent delay equation (1.3) and obtain a constant-delay equation with many delays and a remainder term which is small for solutions in the center or unstable manifolds.

To describe the expansion of the nonlinearity in (1.3) it is convenient to define the difference operator L that generates the linear terms on the right-hand side of (1.11) as

$$(2.1) \quad Lu(t) \equiv -\gamma u(t) - \kappa_1 u(t - a_1) - \kappa_2 u(t - a_2).$$

The difference operator L can be applied recursively, and it will be useful below to note that

$$(2.2) \quad \begin{aligned} L^2 u(t - a_i) &= -\gamma Lu(t - a_i) - \sum_{j=1}^2 \kappa_j Lu(t - a_i - a_j) \\ &= \gamma^2 u(t - a_i) + 2\gamma \sum_{j=1}^2 \kappa_j Lu(t - a_i - a_j) + \sum_{j,m=1}^2 \kappa_j \kappa_m u(t - a_i - a_j - a_m). \end{aligned}$$

Theorem 2.1. *For functions u in the center or unstable manifold of the steady state $u(t) = 0$, the state-dependent delay equation (1.3) can be written as a constant-delay equation up to fourth order as*

$$(2.3) \quad \begin{aligned} u'(t) &= Lu(t) + \sum_{i=1}^2 \kappa_i cu(t) Lu(t - a_i) + \sum_{i,j=1}^2 \kappa_i \kappa_j c^2 u(t) u(t - a_i) Lu(t - a_i - a_j) \\ &\quad - \frac{1}{2} (cu(t))^2 \sum_{i=1}^2 \kappa_i L^2 u(t - a_i) + \mathcal{R}(t), \end{aligned}$$

with $\mathcal{R}(t) = \mathcal{O}(\|u\|_5^4)$, where $\|u\|_5 = \sup_{\theta \in [-5a_2, 0]} |u(\theta)|$.

Proof. Recall from (1.8) that delays are globally bounded by $\tau = a_2 + a_1(\kappa_1 + \kappa_2)/\gamma$ for the state-dependent DDE (1.3). Since $a_2 > a_1$ for $|u| < \delta$, we obtain the stronger bound that $t - \alpha_j(t, u(t)) \leq a_2 + c\delta$. Now consider u in the center or unstable manifold so that solutions can be extended in the past. Using (2.1), we can rewrite (1.11) as $u'(t) = Lu(t)$, and (1.3) as

$$(2.4) \quad u'(t) = Lu(t) - \sum_{i=1}^2 \kappa_i [u(t - a_i - cu(t)) - u(t - a_i)].$$

As already noted, the only nonlinearities in (1.3) arise from the state dependence of the delays, and we must handle these terms carefully to obtain a correct expansion for the normal form. Close to steady state and close to Hopf bifurcation, the state-dependent part of the delay term, $-cu(t)$, will be close to zero. Therefore, close to the bifurcation the term $t - a_i - cu(t)$ represents a small displacement from the constant delay $t - a_i$. Since we assume $a_i > 0$, the perturbation will not be singular.

We write Taylor's theorem as

$$(2.5) \quad \begin{aligned} u^{(p)}(w - \tau - cu(w)) &= u^{(p)}(w - \tau) + \int_0^1 u^{(p+1)}(w - \tau - cu(w) s_1) ds_1 (-cu(w)) \\ &= u^{(p)}(w - \tau) + u^{(p+1)}(w - \tau) (-cu(w)) \\ &\quad + \int_0^1 \int_0^{s_1} u^{(p+2)}(w - \tau - cu(w) s_1 s_2) ds_2 (-cu(w) s_1) ds_1 (-cu(w)) \\ &= \sum_{j=0}^k \frac{1}{j!} u^{(p+j)}(w - \tau) (-cu(w))^j \\ &\quad + \left(\int_0^1 \int_0^{s_1} \dots \int_0^{s_{k-1}} u^{(p+j+1)}(w - \tau - cu(w) s_1 s_2 \dots s_k) \right. \\ &\quad \left. \cdot [s_1(s_1 s_2) \dots (s_1 \dots s_k)] ds_k \dots ds_1 \right) \cdot (-cu(w))^{j+1}, \end{aligned}$$

where we note that on the unstable and center manifolds solutions are C^p , because they can be extended backwards in time; the delays are bounded, and solutions become more regular as we integrate (1.3) forwards in time. Equation (2.5) gives an estimate of the residue of Taylor's theorem in terms of $(-cu(w))^{j+1}$ and $u^{(p+j+1)}$. Now, we use (2.5) with $w = t$, $\tau = a_i$, $p = 0$, and $k = 2$ to obtain

$$(2.6) \quad \begin{aligned} u'(t) &= Lu(t) - \sum_{i=1}^2 \kappa_i \sum_{j=1}^2 \frac{1}{j!} u^{(j)}(t - a_i) (-cu(t))^j \\ &\quad + \left[\sum_{i=1}^2 \kappa_i \int_0^1 \int_0^{s_1} \int_0^{s_2} u^{(3)}(t - a_i - cu(t) s_1 s_2 s_3) s_1^3 s_2^2 s_3 ds_3 ds_2 ds_1 \right] (-cu(t))^3. \end{aligned}$$

Note that we choose $k = 2$ so that the integral remainder term is quartic; more precisely, it is $\mathcal{O}([u(t)]^3 u^{(3)}(t))$. But with bounded delays it follows from differentiating (1.3) that for $\delta > 0$

sufficiently small

$$(2.7) \quad |u^{(3)}(t - a_i - c\delta)| \leq C_2 \sup_{\theta \in [-a_i - a_2 - 2c\delta, 0]} |u''(\theta)| \leq C_3 \sup_{\theta \in [-3a_2 - 3c\delta, 0]} |u'(\theta)| \\ \leq C_4 \sup_{\theta \in [-4a_2 - 4c\delta, 0]} |u(\theta)| \leq C_4 \|u\|_5.$$

One problem with the expansion (2.6) is that the nonlinear terms include delayed derivative terms in u' , u'' , and $u^{(3)}$. We want to eliminate terms of this form to avoid the possibility of neutrality in our equations. To this end, we consider first the terms of the form $u'(t - a_i)$ appearing in (2.6). Applying (1.3) gives

$$u'(t - a_i) = -\gamma u(t - a_i) - \sum_{j=1}^2 \kappa_j u(t - a_i - a_j - cu(t - a_i)).$$

To remove the state dependence from the right-hand side, we apply (2.5) with $w = t - a_i$, $\tau = a_j$, $p = 0$, and $k = 1$ to obtain

$$(2.8) \quad u'(t - a_i) = -\gamma u(t - a_i) - \sum_{j=1}^2 \kappa_j u(t - a_i - a_j) + \sum_{j=1}^2 \kappa_j cu'(t - a_i - a_j)u(t - a_i) \\ + \left[\sum_{j=1}^2 \kappa_j \int_0^1 \int_0^{s_1} u''(t - a_i - a_j - cu(t - a_i)s_1)s_1 ds_2 ds_1 \right] (-cu(t - a_i))^2.$$

But using (1.3) again and (2.5) with $w = t - a_i - a_j$, $\tau = a_m$, and $p = k = 0$, we have

$$(2.9) \quad u'(t - a_i - a_j) = -\gamma u(t - a_i - a_j) - \sum_{m=1}^2 \kappa_m u(t - a_i - a_j - a_m - cu(t - a_i - a_j)) \\ = -\gamma u(t - a_i - a_j) - \sum_{m=1}^2 \kappa_m u(t - a_i - a_j - a_m) \\ + \left[\sum_{m=1}^2 \kappa_m \int_0^1 u'(t - a_i - a_j - a_m - cu(t - a_i - a_j)s_1) ds_1 \right] (-cu(t - a_i - a_j)).$$

Hence, we can rewrite (2.6) as

$$(2.10) \quad u'(t) = Lu(t) + N_2u(t) + N_{23}u(t) - \frac{1}{2} \sum_{i=1}^2 \kappa_i u''(t - a_i)(cu(t))^2 + \mathcal{R}_{24}(t),$$

where $N_2u(t)$ contains the quadratic terms in the expansion of nonlinearity, and $N_{23}u(t)$ contains the cubic terms arising from the substitution of (2.9) and (2.8) into (2.6), with

$$(2.11) \quad N_2u(t) = \sum_{i=1}^2 \kappa_i cu(t) \left[-\gamma u(t - a_i) - \sum_{j=1}^2 \kappa_j u(t - a_i - a_j) \right] = \sum_{i=1}^2 \kappa_i cu(t) Lu(t - a_i),$$

$$(2.12) \quad N_{23}u(t) = \sum_{i,j=1}^2 \kappa_i \kappa_j c^2 u(t) u(t - a_i) \left[-\gamma u(t - a_i - a_j) - \sum_{m=1}^2 \kappa_m u(t - a_i - a_j - a_m) \right] \\ = \sum_{i,j=1}^2 \kappa_i \kappa_j c^2 u(t) u(t - a_i) Lu(t - a_i - a_j).$$

The expression $\mathcal{R}_{24}(t)$ contains the fourth-order integral remainder term of the Taylor series stated in (2.6), as well as the additional fourth-order integral terms arising from the substitution of (2.8) and (2.9) into (2.6).

It remains to expand the terms $u''(t - a_i)$ in (2.10). Differentiating (1.3) and then applying (2.5) with $p = 1$ and $k = 0$ gives

$$(2.13) \quad u''(t - a_i) = -\gamma u'(t - a_i) - (1 - cu'(t - a_i)) \sum_{j=1}^2 \kappa_j u'(t - a_i - a_j - cu(t)) \\ = -\gamma u'(t - a_i) - (1 - cu'(t - a_i)) \sum_{j=1}^2 \kappa_j \left[u'(t - a_i - a_j) \right. \\ \left. + \int_0^1 u'(t - a_i - a_j - cu(t - a_i) s_1) ds_1 (-cu(t - a_i)) \right].$$

Similar to (2.8) and (2.9), but this time applying (2.5) with $p = k = 0$, we can remove the $u'(t - a_i)$ and $u'(t - a_i - a_j)$ terms from (2.13). Just considering the linear terms in (2.13) and using (2.2) we find that

$$\begin{aligned}
& -\gamma u'(t - a_i) - \sum_{j=1}^2 \kappa_j u'(t - a_i - a_j) \\
&= -\gamma \left[-\gamma u(t - a_i) - \sum_{j=1}^2 \kappa_j u(t - a_i - a_j - cu(t - a_i)) \right] \\
&\quad - \sum_{j=1}^2 \kappa_j \left[-\gamma u(t - a_i - a_j) - \sum_{m=1}^2 \kappa_m u(t - a_i - a_j - a_m - cu(t - a_i - a_j)) \right] \\
&= -\gamma \left[-\gamma u(t - a_i) - \sum_{j=1}^2 \kappa_j \left[u(t - a_i - a_j) \right. \right. \\
&\quad \left. \left. + \int_0^1 u'(t - a_i - a_j - cu(t - a_i)s_1) ds_1 (-cu(t - a_i)) \right] \right] \\
&\quad - \sum_{j=1}^2 \kappa_j \left[-\gamma u(t - a_i - a_j) - \sum_{m=1}^2 \kappa_m \left[u(t - a_i - a_j - a_m) \right. \right. \\
&\quad \left. \left. + \int_0^1 u'(t - a_i - a_j - a_m - cu(t - a_i - a_j)s_1) ds_1 (-cu(t - a_i - a_j)) \right] \right] \\
&= L^2 u(t - a_i) + \sum_{j=1}^2 \gamma \kappa_j \int_0^1 u'(t - a_i - a_j - cu(t - a_i)s_1) ds_1 (-cu(t - a_i)) \\
&\quad + \sum_{j,m=1}^2 \kappa_j \kappa_m \int_0^1 u'(t - a_i - a_j - a_m - cu(t - a_i - a_j)s_1) ds_1 (-cu(t - a_i - a_j)).
\end{aligned}$$

Hence, from (2.10) we obtain (2.3), where the remainder term $\mathcal{R}(t)$ contains all the integral terms derived above. Equation (2.7) can be used to show that the remainder term in (2.6) is $\mathcal{O}(\|u\|_5^4)$, and all the remaining integral remainder terms are seen to be $\mathcal{O}(\|u\|_5^4)$ similarly. ■

Overall, we have transformed the state-dependent DDE (1.3) into DDE (2.3), whose terms up to order three contain only constant delays. The price for doing this is the introduction of additional delay terms. While (1.3) contains two state-dependent delays, and its linearization contains two constant delays, in (2.3) the second-order terms features five and the third-order terms nine constant delays. Indeed, it is easy to see that, if we continued the expansion in (2.6) to higher order, then the term $-(-cu(t)^j) \sum_{i=1}^2 \kappa_i u^{(j)}(t - a_i)$ leads to a j th-order term of the form $-(-cu(t)^j) \sum_{i=1}^2 \kappa_i L^j u(t - a_i)$. Thus, when a_1 and a_2 are not rationally related, we will obtain $j(j+3)/2$ delays at j th order, namely, all the terms of the form $u(t - ma_1 - na_2)$ where m, n are nonnegative integers and $1 \leq m + n \leq j$. Recalling that $a_2 > a_1$, the largest delay appearing at j th order is then $u(t - ja_2)$.

If desired, the derivatives of u that appear in $\mathcal{R}(t)$ can all be removed by using (1.3) and derivatives of that equation, just as we removed such derivatives from the lower-order terms. This would result in state-dependent delays appearing in $\mathcal{R}(t)$. Alternatively the state dependence or distributed delay terms could be moved to higher-order terms by truncating

the expansions above at higher order. Importantly, the remainder terms are beyond the orders that we will need for subsequent normal form consideration, and we have the following.

Conjecture 2.2. *The local dynamics near the steady state $u(t) = 0$ of the state-dependent delay equation (1.3) are determined solely by the constant-delay expansion up to the given order. In other words, to study steady-state bifurcations of (1.3), standard normal form calculations for constant-delay DDEs can be applied to the constant-delay expansion truncated to suitable order.*

Specifically for the Hopf-Hopf bifurcations of interest, from now on we consider only the constant-delay DDE we derived to third order in (2.3). Not using the difference operator L , it takes the form

$$\begin{aligned}
 (2.14) \quad u'(t) = & -\gamma u(t) - \kappa_1 u(t - a_1) - \kappa_2 u(t - a_2) - \sum_{i=1}^2 \kappa_i c u(t) \left[\gamma u(t - a_i) + \sum_{j=1}^2 \kappa_j u(t - a_i - a_j) \right] \\
 & - \sum_{i,j=1}^2 \kappa_i \kappa_j c^2 u(t) u(t - a_i) \left[\gamma u(t - a_i - a_j) + \sum_{m=1}^2 \kappa_m u(t - a_i - a_j - a_m) \right] \\
 & - \frac{1}{2} (c u(t))^2 \sum_{i=1}^2 \kappa_i \left[\gamma^2 u(t - a_i) + 2\gamma \sum_{j=1}^2 \kappa_j u(t - a_i - a_j) + \sum_{j,m=1}^2 \kappa_j \kappa_m u(t - a_i - a_j - a_m) \right].
 \end{aligned}$$

We remark that this way of writing the constant-delay DDE is convenient for the implementation of the DDE-BIFTOOL normal form computations which require a DDE with constant delays, and in the supplemental material as `sys_cub_rhs` (see M108765_04.zip [local/web 4.59KB]) we provide a DDE-BIFTOOL system definition of (2.14). However, our own Hopf-Hopf normal form code `HHnfDDEsd` works directly from the state-dependent DDE (1.3) and computes (2.14) from (1.3) using symbolic differentiation as the first step in deriving the normal form parameters.

2.2. Center manifold reduction and resulting normal form. The next step is to derive the normal form for the constant-delay DDE (2.14). For constant-delay DDEs there are well established techniques for deriving normal forms through center manifold reductions. To the best of our knowledge, the Hopf-Hopf bifurcation for a constant-delay DDE was first elaborated in Bélair and Campbell [3], but here we follow the derivation of Guo and Wu [23]. The main idea in this construction is to study the restriction of the semiflow of (2.14) to the center manifold at the point of the Hopf-Hopf bifurcation. On the center manifold the flow satisfies an ODE in four-dimensional space. The reduction to normal form for Hopf-Hopf bifurcations of ODEs is well known, and we follow Kuznetsov [51] to determine the type of Hopf-Hopf bifurcation that occurs.

The algebraic steps for determining the normal form are detailed in the supplementary materials (M108765_01.pdf [local/web 322KB]), and we implemented our own MATLAB code `HHnfDDEsd` (see M108765_02.zip [local/web 6.79KB]), which uses symbolic differentiation to compute the expansion of the state-dependent DDE (1.3) described in section 2.1, and then to evaluate the normal form expressions for the resulting constant-delay DDE (2.14). To

determine the location of the codimension-two Hopf-Hopf points under consideration, we start from an approximate location and solve for $(\kappa_1, \kappa_2, \omega_1, \omega_2)$, so that the pair of frequencies $\omega_1 \neq \omega_2$ both solve (1.13) simultaneously for the same pair of parameter values (κ_1, κ_2) . Our auxiliary routine `findHH` (see M108765_02.zip [local/web 6.79KB] and M108765_03.zip [local/web 14.5KB]) uses the MATLAB function `fminsearch` to minimize

$$f(\kappa_1, \omega_1, \kappa_2, \omega_2) = \sum_{j=1}^2 \left(\gamma + \kappa_1 \cos(a_1 \omega_j) + \kappa_2 \cos(a_2 \omega_j) \right)^2 + \left(\omega_j - \kappa_1 \sin(a_1 \omega_j) - \kappa_2 \sin(a_2 \omega_j) \right)^2,$$

since this function contains the real and imaginary parts of two copies of (1.13). In this way, we are able to find the Hopf-Hopf point essentially to machine precision (we use tolerances of 10^{-14}). At the Hopf-Hopf point we then evaluate the derivatives and functions needed to obtain the center manifold coefficients $g_{l_s r k}^j$ in section A.3 of the supplemental materials, where we employ symbolic differentiation to avoid numerical errors. Thus, we expect that our normal form parameter calculations should be accurate essentially to machine precision, and certainly to eight or more significant figures.

Recently, Wage [78] implemented an extension `ddebiftool_nmf` for DDE-BIFTOOL to compute normal form coefficients at local bifurcations of steady states in constant-delay DDEs. This applies a sun-star calculus-based normalization technique to compute the normal form and center manifold coefficients together, as elaborated for constant-delay DDEs by Janssens [37]. The DDE-BIFTOOL implementation applies only to constant-delay DDEs and so cannot be applied directly to (1.3). However, we can use DDE-BIFTOOL to compute the normal forms of the Hopf-Hopf points of the expanded constant-delay DDE (2.14). The difference between the DDE-BIFTOOL implementation (sun-star calculus approach to computing normal form and center manifold coefficients together) and our approach (center manifold reduction first, then compute normal form of resulting ODE system) results in intermediate coefficients being scaled differently, but the final normal form coefficients computed by both methods should agree. For the DDE-BIFTOOL computations it is suggested that one supply a user-defined routine to compute higher-order derivatives. However, with nine delays in the constant-delay DDE (2.14), determining these derivatives would be a formidable task, and so we use the default DDE-BIFTOOL finite-difference derivative approximations. As an error control this computes the normal form coefficients twice with finite difference approximations of different order. However, in our experience this error estimate is often misleading, as the actual errors are usually much larger than the estimate, as we will see in the next section.

2.3. Hopf-Hopf normal forms. We perform the normal form analysis for the parameter values given in (1.10), which are the same as used in Figure 3 and throughout this paper. For these parameter values the locations of the Hopf-Hopf points and the resulting normal form parameters can be found as described in the previous section.

In Table 1 we state the results of five different computations for the first Hopf-Hopf point HH_1 . The normal form parameters ϑ and δ define coefficients in the scaled truncated amplitude equations

$$(2.15) \quad \begin{aligned} \xi_1' &= \xi_1(\mu_1 - \xi_1 - \vartheta \xi_2), \\ \xi_2' &= \xi_2(\mu_2 - \xi_2 - \delta \xi_1), \end{aligned}$$

Table 1

Values of κ_i and ω_i at the Hopf-Hopf bifurcation HH_1 , seen in Figure 3, and the parameters ϑ and δ that define the scaled truncated amplitude equation (2.15). The values in the first column are computed with our MATLAB code `HHnfDDEsd` applied to (1.3), which implements the procedure described in M108765_01.pdf [local/web 322KB]. The other columns are produced with the normal form extension of DDE-BIFTOOL, applied to the constant-delay DDE (2.14) to obtain four different approximations, two on each of the two intersecting branches of Hopf bifurcations, one from a low-order approximation finite difference approximation to the derivatives, and one using a higher-order approximation. The MATLAB code to generate all output is supplied in the supplementary materials.

	Computed normal form	DDE-BIFTOOL			
		H_1 high	H_1 low	H_u high	H_u low
κ_1	2.080920227069894	2.080905301795540		2.080662320398254	
κ_2	3.786800923405767	3.786811738802836		3.786929718494380	
ω_1	2.487102830659818	2.487103286770640		1.582142631415513	
ω_2	1.582152129599611	1.582151566193548		2.487110459273053	
ϑ	5.291049995477200	5.2909997813	5.2909980111	-0.0222756426	-0.0222756534
δ	-0.022289571330147	-0.0222816360	-0.0222817195	5.2909133110	5.2909132195

for $\xi_j \geq 0$, which determine the dynamics and bifurcations seen as $\mu_j = \text{Re}(\lambda_j)$ are varied close to the Hopf-Hopf point where $\mu_1 = \mu_2 = 0$. The derivation of (2.15) is given in M108765_01.pdf [local/web 322KB], culminating in (A.46).

The first column of Table 1 gives the values computed with our `HHnfDDEsd` code described in sections 2.1–2.2; for comparison, the other columns give values computed with DDE-BIFTOOL’s normal form extension. DDE-BIFTOOL finds Hopf-Hopf points by checking along a branch of Hopf bifurcations for where a second pair of characteristic values crosses the imaginary axis. Thus, with DDE-BIFTOOL, it is possible to obtain two different approximations to the same Hopf-Hopf point by searching along each of the two intersecting branches of Hopf points; in Table 1 we give the locations of HH_1 found on the Hopf curves H_1 and H_u (see Figure 3). As noted in section 2.2, when computing derivatives via finite differences, DDE-BIFTOOL provides two different finite difference approximations to give an indication of the error. The parameters ϑ and δ computed on H_1 with the two different finite difference approximations agree to a relative error of about 10^{-6} , indicating that the finite difference approximations are both quite accurate, and similarly on the branch H_u . However, the agreement is not so good when we compare the answers obtained on the two branches. First, we see that the values of ϑ and δ are swapped on the two branches, which is correct and natural. DDE-BIFTOOL takes as ω_1 the value of ω for the Hopf bifurcation occurring on the branch one is searching along, and takes as ω_2 the value of ω for the second pair of characteristic values crossing the imaginary axis. Hence, the values of ω_1 and ω_2 are swapped when the search is switched from one branch to the other, and this results in the values of ϑ and δ also being swapped. However, even after swapping, we see that the values of ϑ and δ calculated by DDE-BIFTOOL agree to only about four significant figures between the two branches. This also indicates the relative accuracy to which the values of κ_1 , κ_2 , ω_1 , and ω_2 for the Hopf-Hopf point agree on the two branches. So it seems that the accuracy of the DDE-BIFTOOL computed normal forms is limited by the accuracy to which DDE-BIFTOOL computes the location of the Hopf-Hopf points, and not by the accuracy to which it computes

Table 2

The locations and the main normal form and amplitude equation parameters at the three Hopf-Hopf points HH_j shown in Figure 3, computed with our MATLAB code `HHnfDDEsd`.

	HH_1	HH_2	HH_3
κ_1	2.080920227069894	5.608860749294630	9.284862308872761
κ_2	3.786800923405767	2.643352614515402	4.403906490530705
ω_1	2.487102830659818	6.608351858283422	10.93073224661102
ω_2	1.582152129599611	1.765757669232216	1.952009077103193
$\tilde{g}_{2100}^1 = \frac{1}{2}g_{2100}^1$	-0.81417665 - 0.00407087i	-8.59821703 - 10.3402562i	8.25785960 - 81.8392092i
$\tilde{g}_{1011}^1 = g_{1011}^1$	-0.72563615 + 0.26699379i	-4.14512262 - 0.48508142i	-20.2850232 + 11.4745454i
$\tilde{g}_{1110}^2 = g_{1110}^2$	-0.45302394 - 0.29997922i	1.74982076 - 7.92866388i	31.0314747 - 74.3567344i
$\tilde{g}_{0021}^2 = \frac{1}{2}g_{0021}^2$	-0.13405924 - 0.29906145i	-1.42981504 - 0.22951923i	-0.26054578 - 0.38071817i
$G_{2100}^1(0)$	-0.69871613 - 0.28257330i	-7.50609582 - 4.15081310i	-16.8534773 - 28.0243853i
$G_{1011}^1(0)$	-0.51573055 - 0.23247968i	-5.26325881 + 0.05175630i	-21.3834727 + 12.4878724i
$G_{1110}^2(0)$	0.01557408 - 0.46117993i	5.55956094 - 2.01536072i	50.3666025 - 66.5262024i
$G_{0021}^2(0)$	-0.09747225 - 0.22785268i	-0.65677277 - 0.20185598i	-0.20383503 + 0.19032437i
p_{11}	-0.698716133454477	-7.506095827847883	-16.853477387548608
p_{12}	-0.515730558790600	-5.263258815778782	-21.383472731028913
p_{21}	0.015574083096158	5.559560941739119	50.366602528819492
p_{22}	-0.097472252054214	-0.656772770545075	-0.2038350368172633
ϑ	5.291049995477200	8.013820078762780	104.90577608695922
δ	-0.022289571330147	-0.740672790388973	-2.9884991311069409

the normal forms themselves.

We can also swap the ω_j in the computation of the normal forms in our code `HHnfDDEsd`. Because of the symmetry between the parameters, for the index $j = 1$ or 2 so that $3 - j$ indicates the other index, swapping the ω values $\omega_j \leftrightarrow \omega_{3-j}$ exchanges ϑ and δ and the other normal form coefficients (see M108765_01.pdf [local/web 322KB]) as follows:

$$g_{lsrk}^j \leftrightarrow g_{rkls}^{3-j}, \quad \tilde{g}_{lsrk}^j \leftrightarrow \tilde{g}_{rkls}^{3-j}, \quad G_{lsrk}^j \leftrightarrow G_{rkls}^{3-j}, \quad p_{ij} \leftrightarrow p_{3-i3-j}.$$

Because we find the Hopf-Hopf point to machine precision and evaluate the derivatives symbolically, when the ω_j are exchanged, we find that the respective normal form coefficients are identical to machine precision. In fact, the idea of swapping the ω_j and checking the normal form coefficients and parameters turned out to be very useful during the checking and debugging of our code.

Table 2 gives the normal form parameters for the first three Hopf-Hopf points HH_j seen in Figure 3, and also some of the more important intermediate coefficients described in M108765_01.pdf [local/web 322KB]. Here we report only one set of normal form parameters for each Hopf-Hopf point HH_j computed with our MATLAB code `HHnfDDEsd`. We always take $\omega_1 > \omega_2$, and since the period of the periodic orbit bifurcating from the curve H_u is always the largest, this corresponds to taking ω_1 as the frequency of the Hopf bifurcation H_j for $j = 1, 2$, or 3 and ω_2 as the frequency of the Hopf bifurcation H_u . Our normal form calculations give the following overall result.

Proposition 2.3. *At each of the three Hopf-Hopf points HH_1, HH_2 , and HH_3 the following hold:*

- (i) $p_{11} < 0$ and $p_{22} < 0$, which means that normal form coefficients ϑ and δ are sufficient to determine the type of the Hopf-Hopf bifurcation that occurs [51].
- (ii) The nondegeneracy conditions (HH.0)–(HH.6) in supplementary file M108765_01.pdf [local/web 322KB] hold.
- (iii) $\vartheta > 0 > \delta$, which corresponds to subcase III of the simple case as described in section 8.6.2 of [51]; see also Appendix A.5.

In the normal form parameters plane of $(\mu_1, \mu_2) = (\operatorname{Re}(\lambda_1), \operatorname{Re}(\lambda_2))$, Hopf bifurcations occur along the horizontal μ_1 -axis with the bifurcating periodic orbit existing in the upper half plane, and along the vertical μ_2 -axis with the bifurcating periodic orbit existing in the right half plane. Proposition 2.3 implies that there are two curves of torus bifurcations emerging from the origin, which is the codimension-two Hopf-Hopf point: one in the first quadrant and one in the fourth quadrant, with the torus existing in the convex cone between them. On the upper torus bifurcation curve the torus bifurcates from the periodic orbit that exists in the upper half plane, and on the lower torus bifurcation curve it bifurcates from the periodic orbit which exists in the right half plane. The five regions of generic phase portraits are labelled in panel III of Figure 8.25 in [51] (but notice a typo: 13 should be 12), and the corresponding generic phase portraits are given in Figure 8.26 of [51].

Figure 4 shows how our normal form calculations manifest themselves near HH_1 and HH_2 . Panels (a1) and (b1) show the local bifurcation diagrams of the original state-dependent DDE (1.3) as computed with DDE-BIFTOOL [72], consisting of the Hopf bifurcation curve H_u intersecting the Hopf bifurcation curves H_1 and H_2 in HH_1 and HH_2 (as in Figure 3), as well as the associated torus bifurcation curves T_u , T_1 , and T_2 . Panels (a2) and (a3) and panels (b2) and (b3) of Figure 4 show the results of our normal form calculations at HH_1 and HH_2 , respectively. Panels (a3) and (b3) show the positions of the curves of torus bifurcation in the (μ_1, μ_2) -plane of the normal form (2.15). As was discussed, T_u lies in the first quadrant, and the curves T_1 and T_2 each lie in the fourth quadrant. Moreover, the normal form calculations also give the slope of the torus curves in the (μ_1, μ_2) -plane via the actual values of ϑ and δ and (A.50) and (A.51). In particular, T_1 lies very close to H_u near HH_1 in panel (a3), while T_2 is well separated from H_u near HH_2 in panel (b3). Since the Jacobian matrix defined in nondegeneracy condition (HH.6) in Appendix A.5 is invertible at each point HH_j , we can use the coordinate transformation (A.52) to map the (μ_1, μ_2) -plane back to the (κ_1, κ_2) -plane of (1.3). The result is shown in panels (a2) and (b2) of Figure 4, where all curves are actually straight lines that represent the linear approximations, that is, the slopes, of the respective Hopf and torus bifurcation curves near HH_1 and HH_2 . There is excellent correspondence between the nature, order, and slopes of the respective bifurcation curves illustrated in panels (a1) and (a2) and in panels (b1) and (b2), respectively. This fact is clear evidence, over and above the two independent normal form calculations, that Proposition 2.3 is correct and indeed represents the Hopf-Hopf normal form of the full state-dependent DDE (1.3).

Clearly, the bifurcation curves in the local bifurcation diagrams in Figure 4(a1) and (b1) are actually nonlinear, and this explains the visible differences between them and panels (a2) and (b2) further away from HH_1 and HH_2 , respectively. The curvature of these bifurcation curves could be captured by computing higher-order terms in the normal forms, but this is very cumbersome and rarely done. Rather, we will continue these bifurcation curves numerically

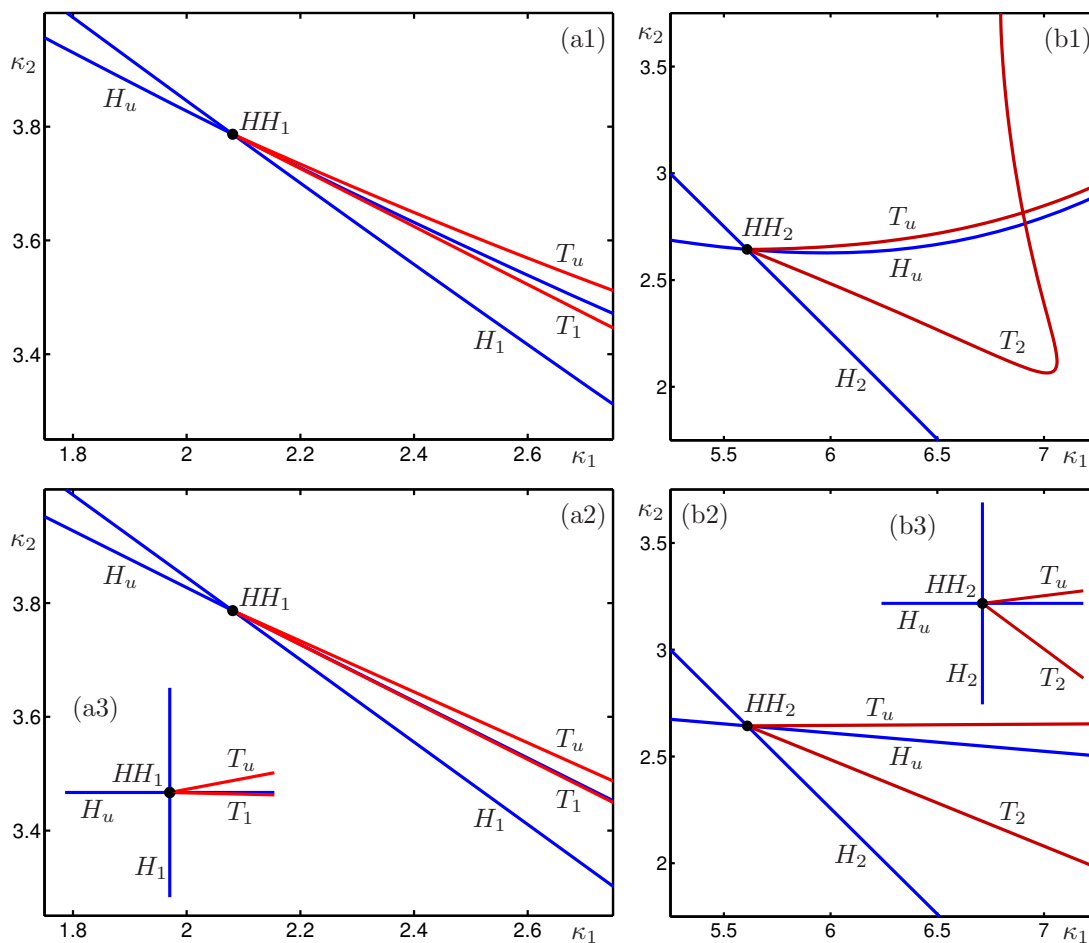


Figure 4. Comparison in the (κ_1, κ_2) -plane near HH_1 and HH_2 between numerically computed torus bifurcation curves for the state-dependent DDE (1.3) (panels (a1) and (b1)), and their linear approximations (panels (a2) and (b2)) obtained by evaluating the normal form coefficients at the respective Hopf-Hopf point and applying the coordinate transformation (A.52). The inset panels (a3) and (b3) show the (μ_1, μ_2) -plane of the normal form (2.15) before this transformation.

with DDE-BIFTOOL more globally throughout the (κ_1, κ_2) -plane. As we will see in the next section, the full bifurcation diagram is very complicated.

3. Structure of bifurcating tori. The existence of Hopf-Hopf bifurcation points that give rise to torus bifurcation curves clearly indicates that (1.3) should feature multifrequency dynamics and, in particular, quasi-periodic and locked dynamics on invariant tori.

Figure 5 shows two examples of dynamics on an invariant torus, which were obtained by numerical integration of (1.3) and after transients have been allowed to die down. The respective dynamics on the torus are illustrated in the left column in projection onto the $(u(t), u(t - a_1), u(t - a_2))$ -space. The right column shows points in the $(u(t - a_1), u(t - a_2))$ -plane whenever $u(t) = 0$; in other words, it shows a two-dimensional projection of the function segments of the Poincaré return map defined by $u(t) = 0$. This representation in the

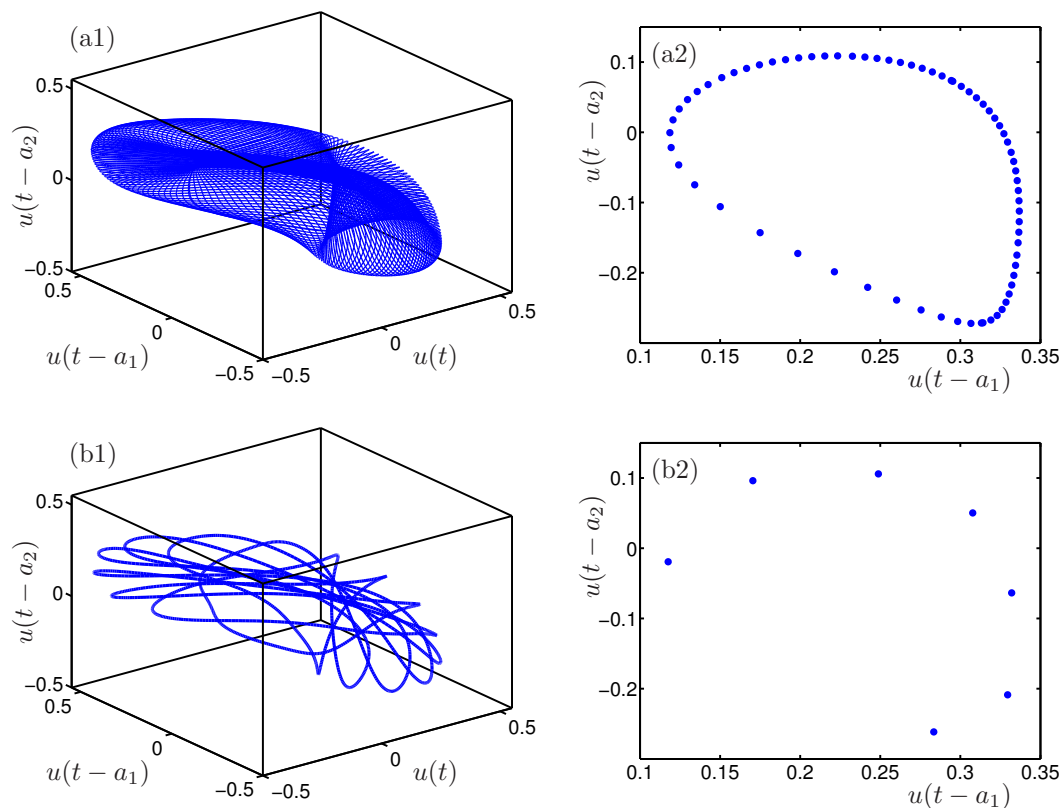


Figure 5. Quasi-periodic torus for $\kappa_1 = 4.44$ in row (a) and $3:7$ phase-locked periodic orbit for $\kappa_1 = 4.409556$ in row (b), where $\kappa_2 = 3.0$. Panels (a1) and (b1) show projections onto $(u(t), u(t - a_1), u(t - a_2))$ -space, and panels (a2) and (b2) the trace in the $(u(t - a_1), u(t - a_2))$ -plane of the Poincaré return map defined by $u(t) = 0$.

$(u(t - a_1), u(t - a_2))$ -plane has been chosen to give a good impression of the low-dimensional character of the tori we encounter, and we refer to it as the Poincaré trace for short; see below for more details on how to construct a Poincaré map of a DDE. In Figure 5(a) the dynamics are quasi-periodic (or of very high period), so that the shown single trajectory covers the torus densely; in the Poincaré trace this corresponds to an invariant closed curve, which is filled out more and more densely as a longer trajectory is computed. An example of locked dynamics on the torus is given in row (b) of Figure 5. More specifically, shown is the attracting periodic orbit on the torus (not shown) in projection onto $(u(t), u(t - a_1), u(t - a_2))$ -space in panel (b1), and the associated Poincaré trace in the $(u(t - a_1), u(t - a_2))$ -plane in panel (b2). They show that the locked periodic orbit forms a $3:7$ torus knot.

Overall, Figure 5 illustrates that two-dimensional invariant tori of (1.3) can be represented conveniently in projection onto the three-dimensional $(u(t), u(t - a_1), u(t - a_2))$ -space and by their Poincaré trace in the $(u(t - a_1), u(t - a_2))$ -plane. We now discuss the choice of Poincaré map for the state-dependent scalar DDE (1.3) in somewhat more detail. It is easy to see that $u \equiv 0$ is the unique steady state of (1.3). Equation (1.8) and the positivity of the parameters implies that any orbit that does not cross $u = 0$ will be eventually monotonic, and also that

$u(t)$ and $u'(t)$ cannot have the same sign on a time interval longer than τ . Hence, since all periodic and quasi-periodic orbits cross $u = 0$, it is natural to use this condition for defining the Poincaré map. More specifically, we define the Poincaré section

$$(3.1) \quad \Sigma = \{\phi \in C : \phi(0) = 0\},$$

which is a codimension-one subspace of the infinite-dimensional phase space C of (1.3). Hence, Σ is infinite-dimensional itself, and the local Poincaré map P_Σ on Σ is defined as the map that takes a downward transversal crossing of zero ($\phi(0) = 0$ with $\phi'(0) < 0$) to the next such crossing. The infinite dimensionality of Σ obscures the structure of the low-dimensional invariant sets (namely, periodic orbits and tori) that we wish to visualize, which is why one considers projections of C and, hence, Σ .

We consider the projection $\mathcal{P} : C \rightarrow \mathbb{R}^3$ via

$$(3.2) \quad \mathcal{P}u_t = (u_t(0), u_t(-a_1), u_t(-a_2)) = (u(t), u(t - a_1), u(t - a_2)) \in \mathbb{R}^3,$$

with corresponding projection

$$(3.3) \quad \mathcal{P}\Sigma = \{(0, u(t - a_1), u(t - a_2))\} \cong \{u(t - a_1), u(t - a_2)\} = \mathbb{R}^2.$$

This generalizes an idea of Mackey and Glass [55], who were the first to project solutions of DDEs into finite dimensions by plotting values of $u(t - \tau)$ against $u(t)$ for a single delay DDE.

For simplicity, we refer to the projected Poincaré section also as Σ , and, throughout, we consider the invariant objects of the local Poincaré map P_Σ defined for points with $u(t) = 0$ and $u'(t) < 0$ (to ensure that there is a unique intersection set for periodic orbits and tori). As was already mentioned, we refer to the respective intersection set in the $(u(t - a_1), u(t - a_2))$ -plane as the Poincaré trace of the invariant object.

We remark that, when the DDE has a sufficient number d of independent variables (at least three), a convenient alternative projection from C to \mathbb{R}^d is obtained by projecting the function segment $u_t \in C$ onto its head-point $u_t(0) = u(t) \in \mathbb{R}^d$. See [22, 47] for an example of this construction for a laser system with $d = 3$. However, this approach is not useful for visualizing the dynamics of (1.3) because u_t is scalar.

Figure 6 illustrates the different projections and representations for the example of the quasi-periodic torus from Figure 5(a). Figure 6(a) shows a different view of the torus in $(u(t), u(t - a_1), u(t - a_2))$ -space together with the Poincaré trace in the local section Σ . This image is very similar to illustrations one finds in the literature of quasi-periodic tori of three-dimensional vector fields; in particular, the torus appears to be smooth, and the intersection curve with Σ is a smooth simple closed curve. That we are in fact dealing with a scalar state-dependent DDE with an infinite-dimensional phase space is illustrated in panels (b) and (c). Figure 6(b) shows the function segments $u_t(\theta)$ corresponding to all the points of the Poincaré trace on Σ in the $u(t - a_1), u(t - a_2)$ -plane of panel (a), that is, the function segments for the points on the torus with $u(t) = 0$ (or equivalently $u_t(0) = 0$) and $u'(t) < 0$. Note that, because the section Σ is defined by the condition $u(t) = 0$, all these function segments are defined over the same fixed time interval $[-a_2, 0] = [-6, 0]$, and all end up at the same point $u(0) = 0$. Figure 6(c) shows a different representation of the function segments associated with the

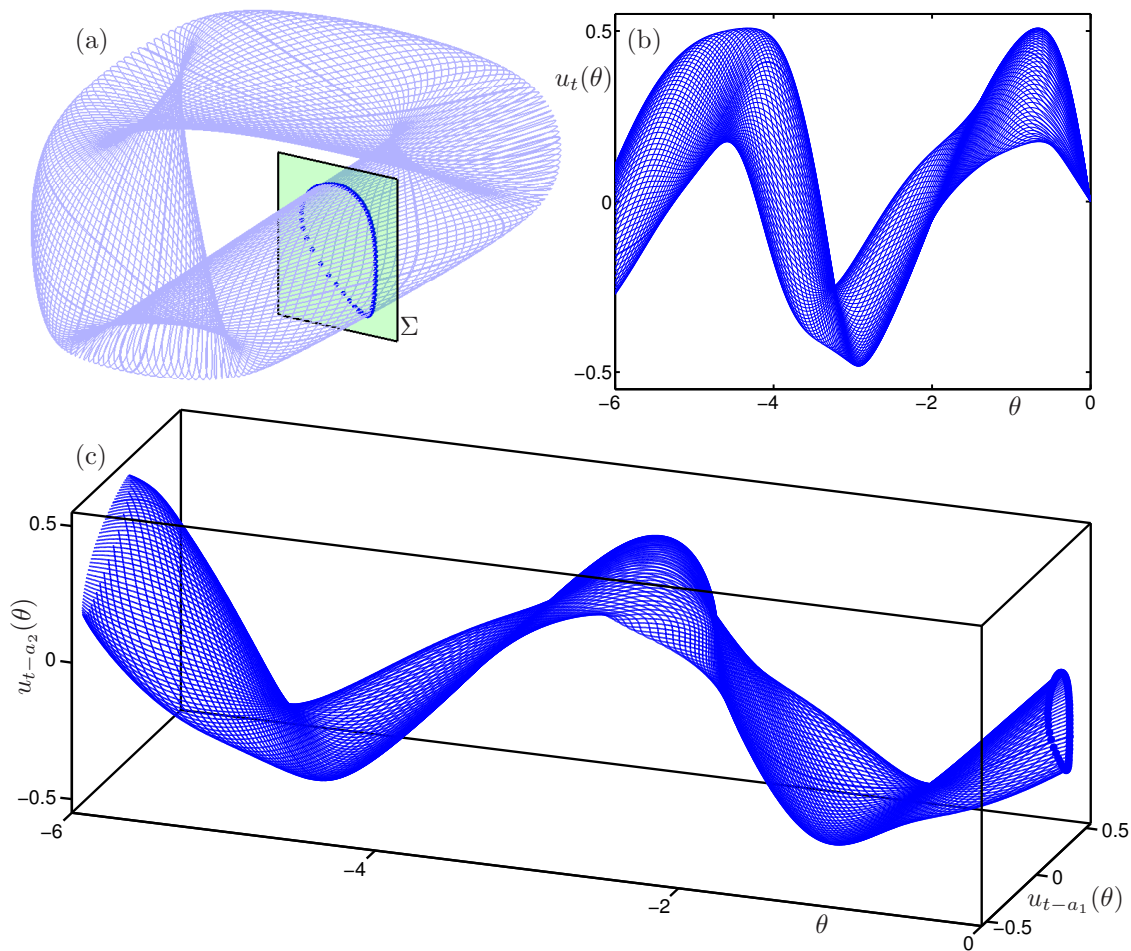


Figure 6. Illustration of Poincaré section and trace for the quasi-periodic torus for $\kappa_1 = 4.44$ and $\kappa_2 = 3.0$ from Figure 5(a). Panel (a) shows the projection onto $(u(t), u(t - a_1), u(t - a_2))$ -space of a single solution of (1.3) on the torus (light blue), together with the trace (blue dots) on the (projected) section Σ (green); the corresponding function segments are shown in panel (b) as functions u_t , and in panel (c) as function segments $(u_{t-a_1}(\theta), u_{t-a_2}(\theta))$, over the delay interval $\theta \in [-6, 0]$. In panel (c) the Poincaré trace is seen in the plane for $\theta = 0$, which corresponds to Σ .

points of the Poincaré trace, with the function segments $(u_{t-a_1}(\theta), u_{t-a_2}(\theta))$ illustrating the “history tails” over the time interval $[-6, 0]$ associated with the trace in (the two-dimensional projection of) Σ . Notice that in this representation the invariant torus appears as a cylinder that is swept out by the function segments in the corresponding orbit under the local Poincaré map P_Σ , with the Poincaré trace seen in the plane for $\theta = 0$ in Figure 6(c).

Figure 7 shows an example of a smooth invariant torus with 1:4 phase-locked dynamics on it. In panels (a)–(c) the torus is represented in the same manner as the quasi-periodic torus in Figure 6. However, in contrast to Figure 5(b), which shows only the locked stable

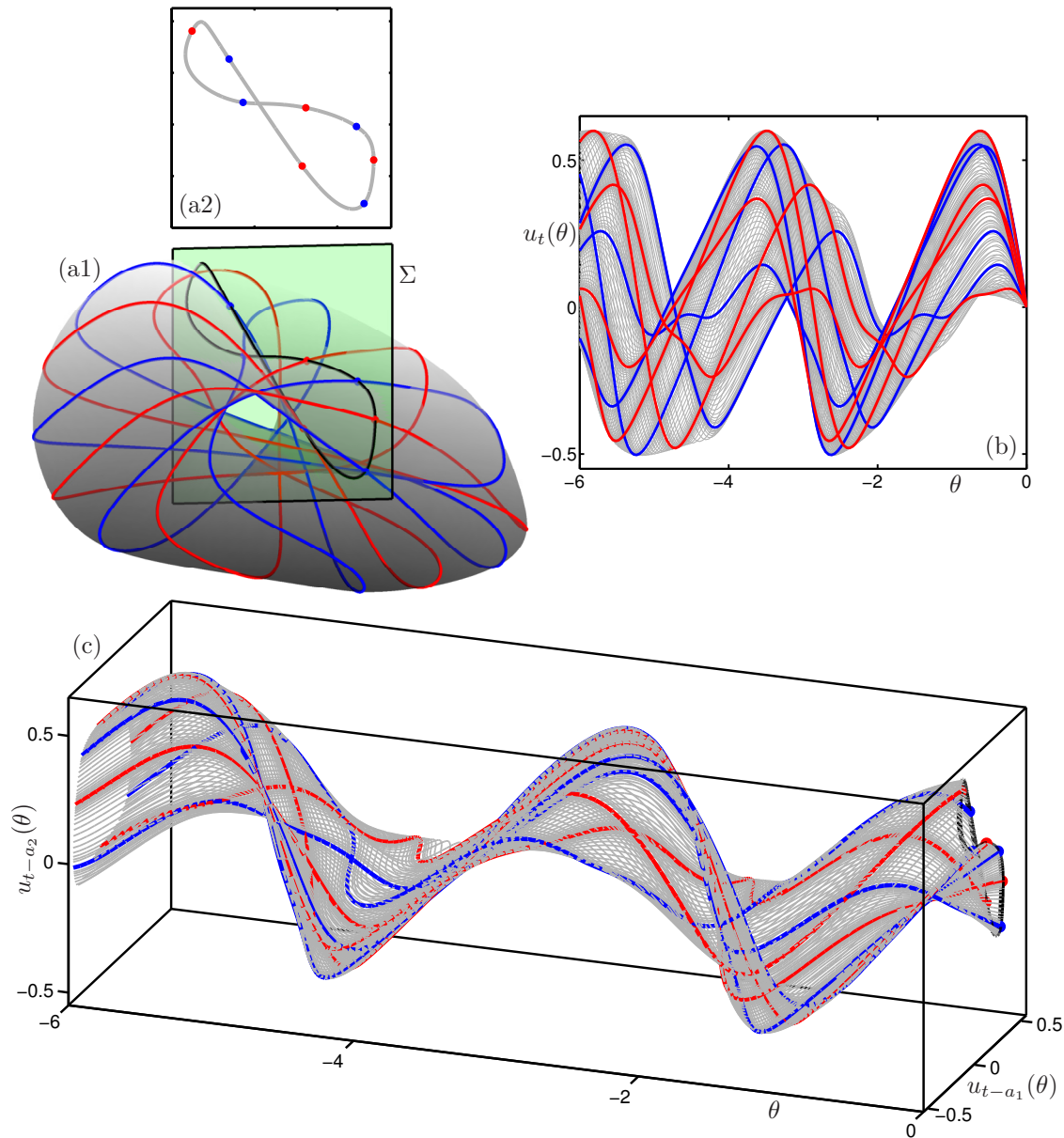


Figure 7. Illustration of Poincaré section and trace for the 1:4 phase-locked torus for $\kappa_1 = 5.405$ and $\kappa_2 = 2.45$. Panel (a1) shows the projection onto $(u(t), u(t - a_1), u(t - a_2))$ -space of the relevant invariant objects, namely, of the stable periodic orbit (blue), the saddle periodic orbit (red), its unstable manifold (grey curve), together with the trace on the (projected) section Σ (green). Panel (a2) shows only the trace of these objects in Σ . The corresponding function segments are shown in panel (b) as functions u_t , and in panel (c) as function segments $(u_{t-a_1}(\theta), u_{t-a_2}(\theta))$, over the delay interval $\theta \in [-6, 0]$.

periodic orbit on the torus, Figure 7 also shows the unstable locked periodic orbit and its two-dimensional unstable manifold, which together form the locked invariant torus itself. Figure 7(a1) shows the torus rendered as a surface in $(u(t), u(t - a_1), u(t - a_2))$ -space with the

stable and unstable locked periodic orbits lying on it. Also shown is the section Σ and the Poincaré trace; for clarity, the trace is shown on its own in the $(u(t - a_1), u(t - a_2))$ -plane in panel (a2). Associated segments u_t are shown as functions of θ in Figure 7(b), and in terms of $(u_{t-a_1}(\theta), u_{t-a_2}(\theta))$ in Figure 7(c).

The torus in Figure 7 gives rise to a single smooth curve as the trace in the $(u(t - a_1), u(t - a_2))$ -plane, on which lie four points of a stable period-four orbit and four points of an unstable period-four orbit; see Figure 7(a2). The stable periodic orbit was found by numerical simulation. It was then used to start a continuation of the periodic orbit in the parameter κ_1 , which yielded, after a fold or saddle-node bifurcation of periodic orbits, the unstable periodic orbit. This calculation also confirmed that, as theory predicts, the unstable periodic orbit has exactly one unstable Floquet multiplier. We extracted the unstable eigenfunction associated with the unstable periodic orbit on the torus and used it to define two initial functions in the local unstable manifold of the periodic orbit (one on each side of the orbit). Then numerical integration near the periodic point and along the unstable eigenfunction was used to compute trajectories that lie on the unstable manifold; associated orbit segments are shown in Figure 7(b) and (c). Careful selection and ordering of orbit segments on the unstable manifolds (between intersections with the Poincaré section) allowed us to render the torus as a surface in $(u(t), u(t - a_1), u(t - a_2))$ -space in Figure 7(a1), and to draw the corresponding one-dimensional curve in the $(u(t - a_1), u(t - a_2))$ -plane in Figure 7(a2).

Again, the representation of locked dynamics on the torus in Figure 7 is very reminiscent of what one would expect to find in a three-dimensional vector field. Notice, however, that—in contrast to the quasi-periodic torus in Figure 6—the invariant curve in the $(u(t - a_1), u(t - a_2))$ -plane has a point of self-intersection. The torus in $(u(t), u(t - a_1), u(t - a_2))$ -space also has a curve of self-intersection; see Figure 7(c). This is due to projection from the infinite-dimensional phase space and a reminder that we are dealing with a DDE and not a low-dimensional dynamical system. While self-intersections may occur, we believe that the chosen Poincaré section Σ defined by $u(t) = 0$ is the most convenient and natural choice for the study of multifrequency dynamics in (1.3).

3.1. Resonance tongues and locked tori. Continuation of the two torus bifurcation curves that are known to emerge from the Hopf-Hopf point HH_1 in the (κ_1, κ_2) -plane shows that the two local curves T_u and T_1 are actually part of a single curve; it is shown in Figure 8. Along the two local branches one finds many points of $p:q$ resonance where the Floquet multiplier is a rational multiple of 2π . They can be detected during the continuation of the torus bifurcation curve, and Figure 8(a) shows such resonances for $q \leq 13$. Emerging from each point of $p:q$ resonance are two curves of fold or saddle-node of periodic orbit bifurcations, which bound a resonance tongue or region where the dynamics on the torus is $p:q$ locked. In Figure 8(a) we find that the pair of saddle-node of periodic orbit bifurcation curves emerging from each $p:q$ resonance point on the upper branch T_u can be continued to a $p:(p+q)$ resonance point on the lower branch T_1 . The enlargement in panel (b) shows this for the specific example of the 2:7 resonance on T_u and the 2:9 resonance on T_1 ; the further enlargement in Figure 8(c) shows the narrow tip of the resonance tongue near the 2:7 resonance point.

Such “connected resonance tongues” near a Hopf-Hopf bifurcation point are a curious phenomenon that has not been reported elsewhere to the best of our knowledge. Note that

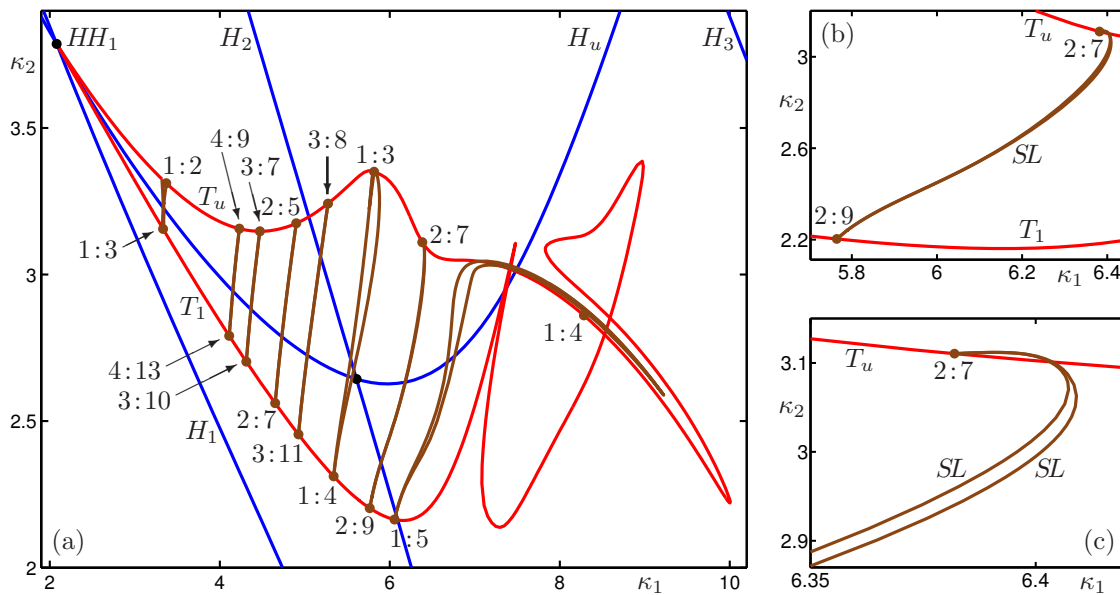


Figure 8. (a) The torus bifurcation curves T_u and T_1 emerging from the Hopf-Hopf bifurcation point HH_1 and associated resonance tongues in the (κ_1, κ_2) -plane. Panels (b) and (c) are successive enlargements of the resonance tongue that connects a $2:7$ resonance on T_u with a $2:9$ resonance on T_1 .

general theory (for ODEs and DDEs with fixed delays) states that the existence of smooth (normally hyperbolic) invariant tori—with locked dynamics in resonance tongues and quasi-periodic dynamics along curves in the (κ_1, κ_2) -plane—is guaranteed only locally near the curves T_u and T_1 . Since, a $p:q$ torus knot is topologically different from a $p:(p+q)$ torus knot, the respective locked solutions near T_u and T_1 cannot lie on one and the same smooth invariant torus. Nevertheless, a locked solution on a torus is simply a periodic orbit, and it may continue to exist even when the underlying torus disappears. When no longer constrained to lie on an invariant torus, a $p:q$ periodic orbit can be transformed smoothly into a $p:(p+q)$ periodic orbit, which explains why the saddle-node of periodic orbit bifurcation curves may connect the respective points on T_u and T_1 . It is important to realize, however, that the regions that the pair of curves bound cannot contain smooth invariant tori throughout; some examples of nonsmooth tori will be presented in section 3.2. The questions of how the smooth tori near T_u and T_1 break up and how the overall phenomenon is organized by the Hopf-Hopf bifurcation certainly merit further study, ideally in the setting of a four-dimensional ODE.

Near the points of resonances on T_u and T_1 the respective locked dynamics must be expected to take place on a smooth invariant torus; indeed, Figure 7 is an example of such a smooth torus with locked dynamics. Figure 9(a) shows an enlargement of the resonance tongue that connects a $1:3$ resonance on T_u with a $1:4$ resonance on T_1 , and panel (b) shows the continuation of the corresponding locked periodic orbits for $\kappa_2 = 3$. There are three branches of stable and three branches of unstable periodic solutions in Figure 9(b), which meet at saddle-node bifurcations marking the left and right boundaries of this region of locking. Tori beyond the resonance region in panel (b) feature dynamics that is quasi-

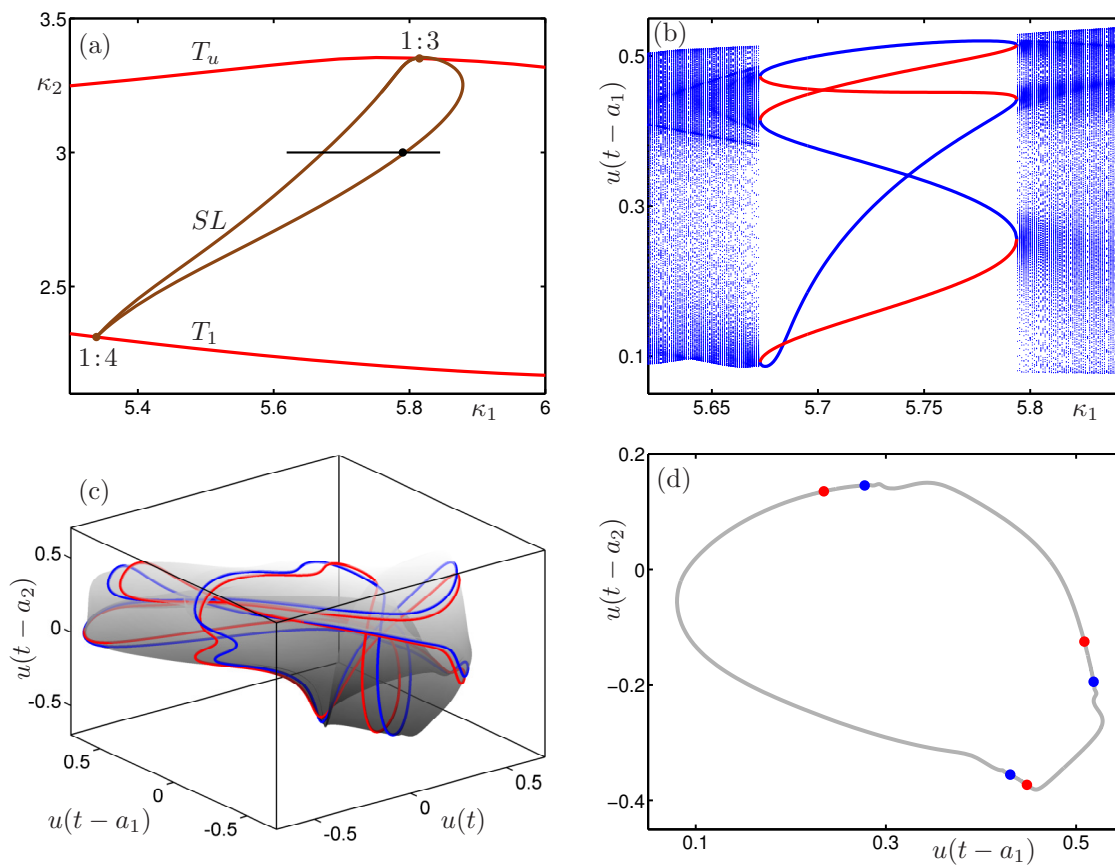


Figure 9. The resonance tongue that connects a 1:3 resonance on T_u with a 1:4 resonance on T_1 . Panel (a) shows this resonance tongue in the (κ_1, κ_2) -plane. Panel (b) is a one-parameter bifurcation diagram in κ_1 for fixed $\kappa_2 = 3.0$, showing the values of $u(t - a_1)$ of the Poincaré trace of the stable periodic orbit (blue) and of the saddle periodic orbit (red) inside the resonance tongue, and of other solutions on tori outside the resonance tongue. Panel (c) shows the 1:3 phase-locked torus (grey) for $\kappa_1 = 5.79$ with the stable and saddle periodic orbits in projection onto $(u(t), u(t - a_1), u(t - a_2))$ -space, and panel (d) is its Poincaré trace in the $(u(t - a_1), u(t - a_2))$ -plane. The accompanying animation (M108765_06.avi [local/web 3.45MB]) shows the corresponding evolution of the Poincaré trace over the κ_1 -range in panel (b).

periodic or of very high period; these tori were found by parameter sweeping with numerical integration. Figure 9(c) shows the invariant torus for $\kappa_1 = 5.79$ (near the right boundary of the locking region) as a surface in $(u(t), u(t - a_1), u(t - a_2))$ -space, and panel (d) is its trace for the Poincaré map defined by $u(t) = 0$. The torus was again found by computing the one-dimensional unstable manifolds of the saddle periodic orbits. As Figure 9(c) and (d) indicate clearly, this invariant torus is 1:3 locked and smooth. The animation M108765_06.avi [local/web 3.45MB] shows the evolution of the Poincaré trace as the parameter κ_1 is swept over the range shown in Figure 9(b).

On the other hand, the saddle-node of periodic orbit bifurcation curves in Figure 8(a) connect a $p : q$ resonance point on T_u to a $p : (p + q)$ resonance point on T_1 . Hence, the torus inside the respective resonance tongue cannot be smooth throughout, because the knot

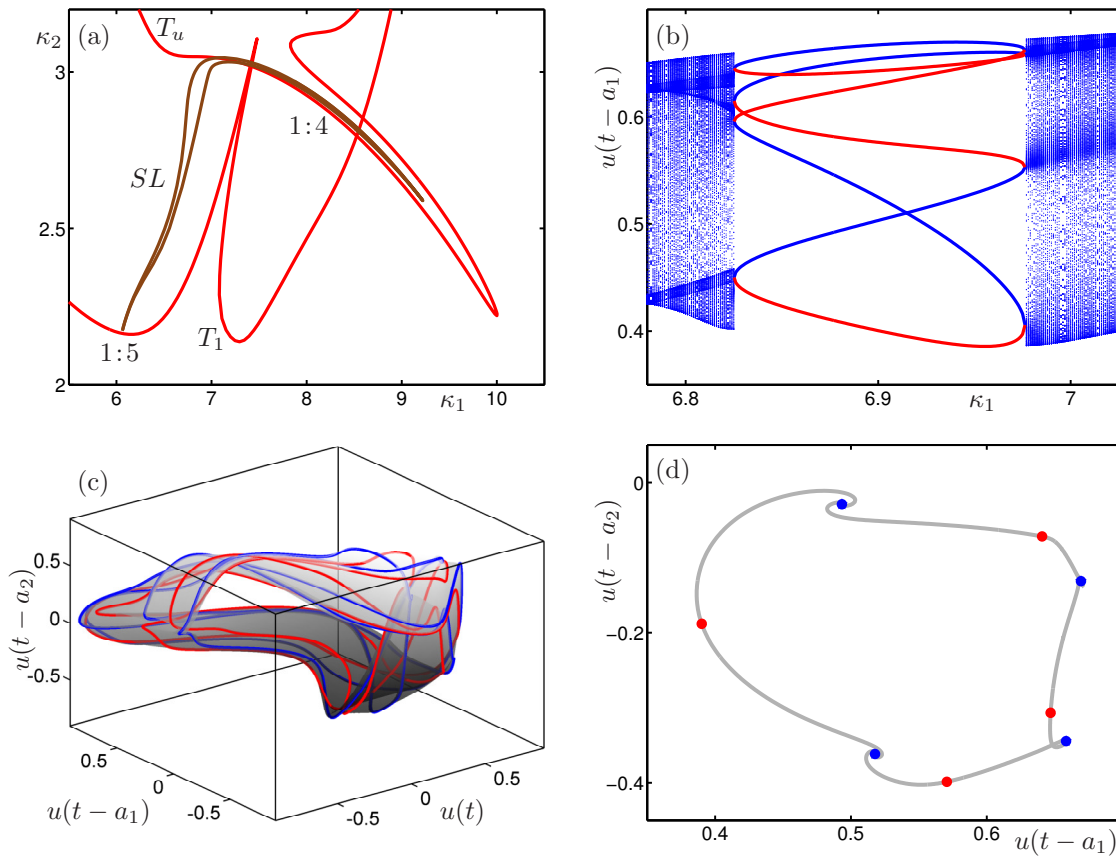


Figure 10. The resonance tongue that connects a 1:4 resonance on T_u with a 1:5 resonance on T_1 . Panel (a) shows this resonance tongue in the (κ_1, κ_2) -plane. Panel (b) is a one-parameter bifurcation diagram in κ_1 for fixed $\kappa_2 = 3.0$, showing the values of $u(t - a_1)$ of the Poincaré trace of the stable periodic orbit (blue) and of the saddle periodic orbit (red) inside the resonance tongue, and of other solutions on tori outside the resonance tongue. Panel (c) shows the 1:4 phase-locked torus-like object (grey) for $\kappa_1 = 6.93$ with the stable and saddle periodic orbits in projection onto $(u(t), u(t - a_1), u(t - a_2))$ -space, and panel (d) is its Poincaré trace in the $(u(t - a_1), u(t - a_2))$ -plane. The accompanying animation (M108765_07.avi [local/web 4.19MB]) shows the corresponding evolution of the Poincaré trace over the κ_1 -range in panel (b).

type on a smooth invariant two-torus is an invariant. While a $p:q$ periodic orbit can change smoothly into a $p:(p+q)$ periodic orbit—as Figure 8 shows—this cannot happen on one and the same smooth two-torus.

Figure 10(a) shows an enlargement of the resonance tongue that connects a 1:4 resonance on T_u with a 1:5 resonance on T_1 . The one-parameter bifurcation diagram for $\kappa_2 = 3.0$ in Figure 10(b) shows that one is dealing with 1:4 locking: there are four branches each of stable and unstable periodic orbits, which meet in saddle-node bifurcations at the boundary of the resonance tongue; the dynamics beyond the tongue is again quasi-periodic or of very high period. The situation looks exactly as that near the 1:3 resonance point in Figure 9(b). However, as Figure 10(c) and (d) show, there is no longer a smooth invariant torus. Rather, the one-dimensional unstable manifold of the saddle periodic orbit spirals around the stable

periodic orbit; see panel (d). This means that the stable periodic orbit has developed a pair of complex conjugate leading Floquet multipliers, which is one mechanism for the loss of normal hyperbolicity of an invariant torus that is known from ODE theory [2]. Note that the loss of normal hyperbolicity is found numerically by two independent computations. The manifold seen to spiral in panel (d) was computed by using the initial value problem solver `ddesd` and its event detection to compute a trajectory in the unstable manifold of the periodic orbit and its intersections with the Poincaré section, revealing the spiralling dynamics. But we also used DDE-BIFTOOL to directly compute the Floquet multipliers of the unstable periodic orbit, confirming that the two dominant multipliers are complex conjugate. The loss of normal hyperbolicity is very clearly seen in the animation M108765_07.avi [local/web 4.19MB], which shows the evolution of the Poincaré trace in a one-parameter κ_1 -sweep across the resonance tongue. Namely, stable periodic points on the Poincaré trace are denoted by stars in the animation when their dominant Floquet multipliers are complex conjugate; this happens across much of this traverse of the resonance tongue, and the unstable manifold of the saddle periodic orbit is then seen to spiral into the stable periodic points on the Poincaré trace.

3.2. Break-up of a 1 : 4 locked torus. In the previous section we discussed the local transition for fixed $\kappa_2 = 3$ through a 1 : 4 resonance as κ_1 changes near $\kappa_1 = 6.93$. Notice in Figure 10(a) that the associated resonance tongue in the (κ_1, κ_2) -plane has the shape of a horseshoe with maxima of the two bounding saddle-node curves at $\kappa_1 \approx 7$. Both of the two maxima occur for $\kappa_2 > 3$. Hence, for $\kappa_2 = 3$ there is a range of κ_1 -values outside this resonance tongue before it is entered again at $\kappa_1 \approx 7.617$ when κ_1 is increased further beyond the range shown in Figure 10(b). As we will show now, the transition through this second part of the 1 : 4 resonance tongue results in the break-up and disappearance of the torus via a complicated scenario of bifurcations that involves nearby periodic orbits.

The sequence of bifurcations for fixed $\kappa_2 = 3$ and the associated dynamics are illustrated by two companion figures. Figure 11 shows two one-parameter bifurcation diagrams in κ_1 , and Figure 12 shows the associated sequence of Poincaré traces in the $u(t - a_1), u(t - a_2)$ -plane; see also the accompanying animation, which animates the evolution of the Poincaré traces for $\kappa_1 \in [7.530, 7.702]$.

Starting at $\kappa_1 = 7.5$, there is an invariant torus with quasi-periodic or high-period solutions on it; see Figure 11(a). As κ_1 is increased, the first bifurcation of interest is the creation of two saddle periodic orbits at a saddle-node bifurcation of periodic orbits at $\kappa_1 \approx 7.5363$. We refer to these as the principal periodic orbits because their branch can actually be traced back to first Hopf bifurcation H_1 ; see Figure 1. As is shown in Figure 11(b), at $\kappa_1 \approx 7.5664$ one of the two saddle periodic orbits gains stability in a torus bifurcation when the branch of periodic orbits crosses the torus curve T_u . This torus bifurcation is close to 1 : 4 resonance, with numerically computed Floquet multipliers $\rho \approx -0.019 \pm 1.000073i$ very close to $\pm i$. There is then an interval of κ_1 -values for which the stable periodic orbit on the principal branch and the stable quasi-periodic torus co-exist; see Figure 11(a). The associated invariant closed curve in the $u(t - a_1), u(t - a_2)$ -plane is shown in Figure 12(a), together with the two points that represent the stable and saddle principal periodic orbits in the Poincaré trace.

At $\kappa_1 \approx 7.5796$ another saddle-node bifurcation of periodic orbits creates a pair of period-

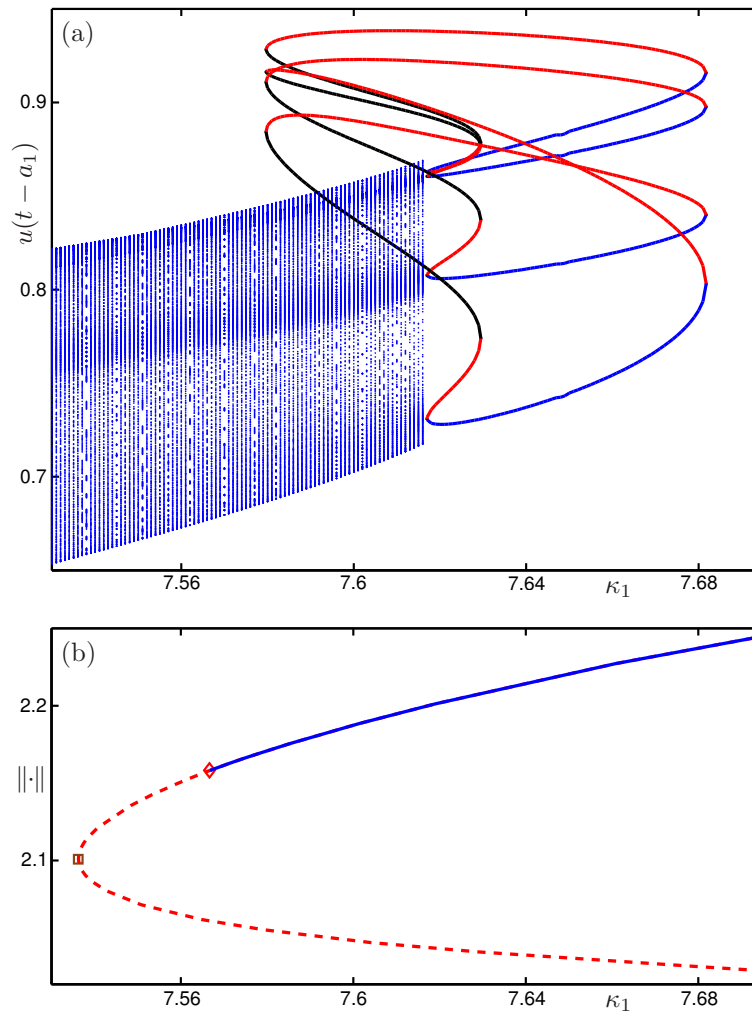


Figure 11. One-parameter bifurcation diagrams relevant for the transition through the 1 : 4 resonance. Panel (a) shows the values of $u(t - a_1)$ of the Poincaré trace of solutions on tori outside the resonance tongue and of period-four periodic orbits that are stable (blue), have one unstable Floquet multiplier (red), or have two unstable Floquet multipliers (black). Panel (b) shows the simultaneously existing pair of principal periodic orbits that are born in a saddle-node bifurcation, and one of which is stable (blue) past the torus bifurcation (diamond).

four orbits, one of which has exactly one and the other two unstable Floquet multipliers; see Figure 11(a). In the Poincaré trace in Figure 12(b), for $\kappa_1 = 7.58$, these are represented by two sets of period-four points. Also shown is the one-dimensional trace of the unstable manifold of the saddle periodic orbit with one unstable Floquet multiplier; note that both its branches (on either side of the respective periodic point) converge to the attracting invariant curve. Almost immediately afterwards, for $7.58 < \kappa_1 < 7.581$, there is a bifurcation that changes the nature of the unstable manifold of the saddle period-four orbit. As Figure 12(c) shows, one branch now goes to the attracting principle periodic orbit (blue star), while the

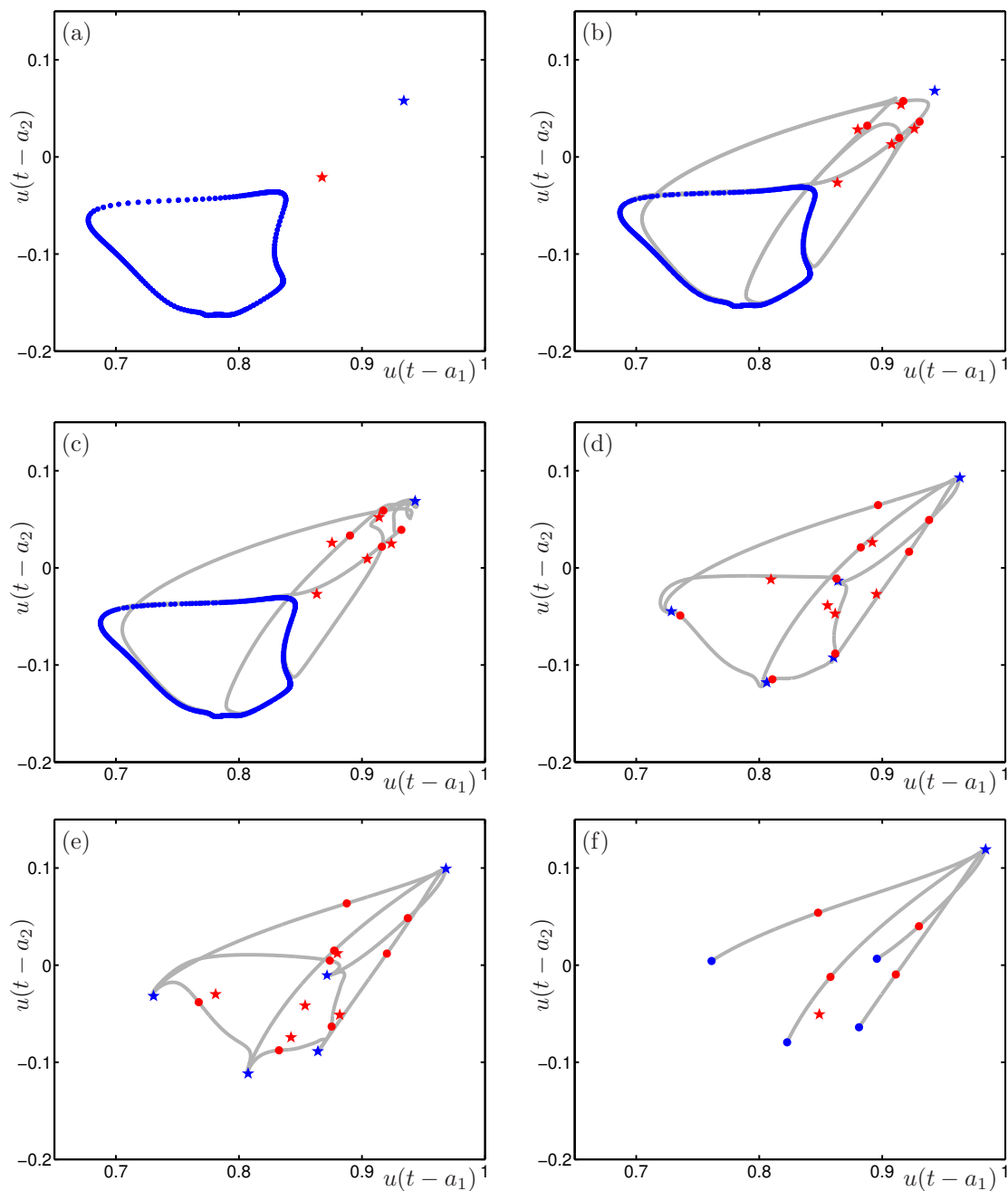


Figure 12. Sequence of Poincaré traces in the $(u(t-a_1), u(t-a_2))$ -plane showing the break-up of a torus with 1:4 phase locking. Shown are invariant curves (bold blue dots), stable periodic points (blue stars) and saddle periodic points with two unstable Floquet multipliers (red stars) or with a single unstable Floquet multiplier (red dots); also shown are the traces of the unstable manifolds (grey curves) of the latter saddle points. Here $\kappa_2 = 3$, and in panels (a)–(f) κ_1 takes the values 7.567, 7.58, 7.581, 7.618, 7.629, and 7.666, respectively. See also the accompanying animation (M108765_08.avi [local/web 2.97MB]).

other branch still goes to the attracting invariant curve. This means that, on the level of the Poincaré trace, we are dealing with a global bifurcation that is described in the approximating normal form of a 1:4 resonance as a saddle connection of square type [44, 45].

At $\kappa_1 \approx 7.617$ the 1:4 resonance tongue is re-entered, and we find two locked period-four orbits on the torus, one of which is attracting and the other of which has a single unstable Floquet multiplier. In the trace in Figure 12(d) they are shown as a further two sets of period-four points. Also shown is the trace of the unstable manifold of the saddle four-periodic orbit on the torus, both branches of which end up at neighboring period-four attracting points to form a smooth invariant curve. Hence, the torus is still normally hyperbolic (that is, smooth), as is expected near the boundary of a resonance tongue. Notice that the respective branch of the unstable manifold of each saddle period-four point off the invariant curve now also goes to the attracting periodic orbit on the torus.

As κ_1 is increased further, the torus loses normal hyperbolicity. More specifically, the branches of all unstable manifolds shown in Figure 12(e) approach the attracting period-four orbit along the same side of its weak stable eigendirection, so that a cusp is formed along the attracting period-four orbit. Moreover, the period-four orbit with two unstable Floquet multipliers, created at $\kappa_1 \approx 7.5796$ and not mentioned since, now enters the action. As κ_1 increases, this saddle periodic orbit approaches the saddle periodic orbit on the torus, which has a single unstable Floquet multiplier. At $\kappa_1 \approx 7.6295$, the two period-four orbits annihilate each other in a further saddle-node bifurcation; see Figure 11(a). The periodic points and the associated unstable manifold disappear at this value of κ_1 . Hence, as Figure 12(f) illustrates, we are left with the two remaining period-four orbits: the attracting one and a saddle periodic orbit. Notice that the unstable manifold of the latter does not change in this process, meaning that one branch of each period-four point in the trace still ends up at the principal periodic orbit, and the other at the respective attracting period-four point. As κ_1 is increased even further, the two period-four orbits approach each other and finally disappear in the last saddle-node bifurcation at $\kappa_1 \approx 7.6818$ in Figure 11(a). Hence, we are left with only the stable and saddle principal periodic orbits; see Figure 11(b).

Overall, the torus loses normal hyperbolicity and then breaks up and disappears completely. In particular, unlike for the cases studied in section 3.1, the torus does not re-emerge on the other side of the 1:4 resonance tongue.

4. Overall bifurcation diagram and conclusions. Our study of the scalar state-dependent DDE (1.3) concentrated on the dynamics associated with the presence of codimension-two Hopf-Hopf bifurcation points. We presented a normal form procedure for state-dependent DDEs that, by eliminating the state dependence up to order three, allowed us to determine the type of Hopf-Hopf bifurcation from the resulting DDE with nine constant delays. In this way, we showed that a pair of torus bifurcation curves emerges locally from each of the three Hopf-Hopf bifurcation points in the region of interest of the (κ_1, κ_2) -plane of (1.3). Our normal form computations have been confirmed by finding and continuing these torus bifurcation curves numerically with the package DDE-BIFTOOL. What is more, numerical continuation allowed us to follow the torus bifurcation curves beyond the local neighborhoods of the Hopf-Hopf bifurcation points, and to identify the structure of resonance tongues emerging from them. We computed locked periodic orbits on the tori and determined the boundaries of resonance

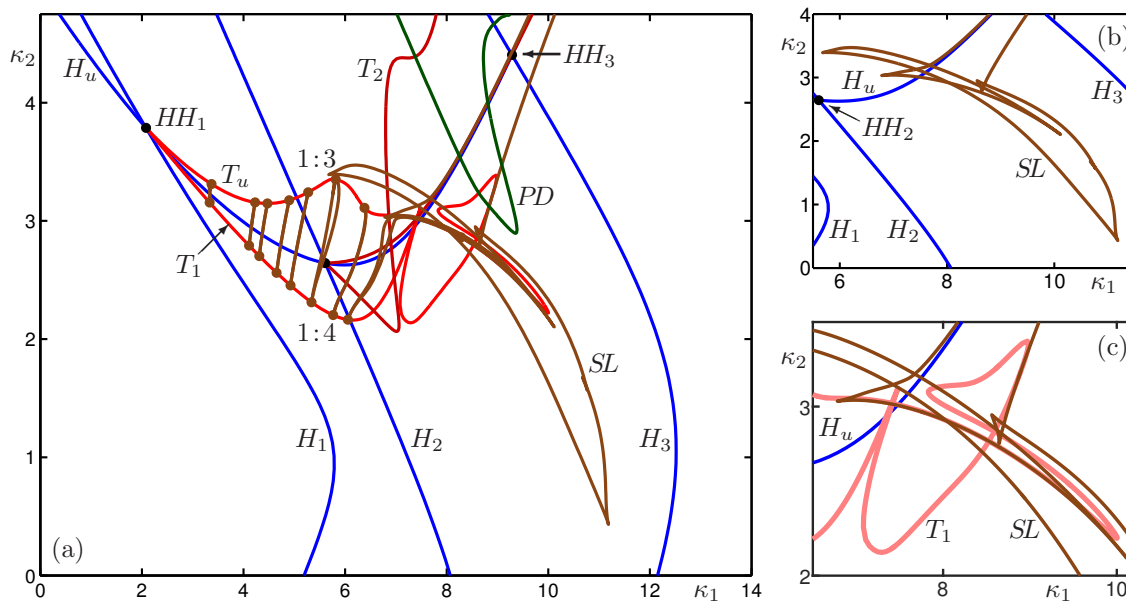


Figure 13. (a) Overall bifurcation diagram of (1.3) in the (κ_1, κ_2) -plane, showing curves of Hopf bifurcation (blue) of torus bifurcation (red), of saddle-node of limit cycle bifurcation (brown), and of period-doubling bifurcation (green). Panel (b) is an enlargement near HH_2 , and panel (c) shows details of the saddle-node of limit cycle bifurcation curve SL that is not connected to a resonance point on a torus.

tongues by continuing their saddle-node bifurcations. The tori and the dynamics on them were investigated and visualized by suitable projections into three-dimensional space, as well as by their two-dimensional Poincaré traces. In particular, we computed the unstable manifolds of saddle-periodic orbits with a single unstable Floquet multiplier, which allowed us to study in considerable detail how invariant tori break up and disappear, for example near a $1 : 4$ resonance.

The starting point of our investigation was the one-parameter bifurcation diagram of Figure 1 from [34]. Specifically, we used it to start continuations of periodic solutions and of bifurcation curves in the (κ_1, κ_2) -plane, namely, the curves of Hopf bifurcation in Figure 3, as well as the curves of torus bifurcation and saddle-node bifurcation that bound certain resonance tongues in Figure 8(a). Returning to Figure 1, one can identify two additional bifurcations that we have not considered yet in our study of resonance phenomena: a period-doubling bifurcation and an additional saddle-node bifurcation of limit cycles. Figure 13 shows the overall two-parameter bifurcation diagram of (1.3) in the (κ_1, κ_2) -plane with all the above bifurcation curves. Panel (a) shows the relevant region where $0 \leq \kappa_1 \leq 14$ and $0 \leq \kappa_2 \leq 4.75$. In particular, shown are the three pairs of torus bifurcation curves emerging from the Hopf-Hopf bifurcation points HH_1 to HH_3 . Notice that the two torus bifurcation curves emerging from HH_3 stay very close to the Hopf bifurcation curve H_u ; similarly, the torus bifurcation curve T_u emerging from HH_2 stays close to H_u , while the other curve T_2 exits the top of the (κ_1, κ_2) -plane. Prominent in panel (a) is the curve PD of period-doubling bifurcation, which has a minimum near $(\kappa_1, \kappa_2) \approx (10, 3)$. As Figure 1(a) shows, the periodic orbit undergoing

the period-doubling bifurcation has a large amplitude.

The other new curve in Figure 13 is the saddle-node of limit cycle bifurcation curve labelled SL . It enters and exits the top of the (κ_1, κ_2) -plane near and in the direction of the Hopf bifurcation curve H_u . As panel (b) shows, the curve SL is very complicated and features eight cusps (two pairs of which are actually very close to swallowtail bifurcations), resulting in quite a number of regions with different numbers of bifurcating periodic orbits. From section 3.2 it is clear that some periodic orbits emerging from saddle-node bifurcations play an important role in the torus break-up mechanism. At the same time, the overall bifurcation diagram in Figure 13 shows with the example of SL that there are other saddle-node bifurcations that may not immediately be related to the torus bifurcations emerging from HH_1 to HH_3 . However, SL comes very close to several torus bifurcation curves; see Figure 13(c). Moreover, it closely follows the horseshoe-shaped resonance region (discussed in section 3.2) that connects the 1:4 resonance on T_u with the 1:5 resonance in T_1 . We remark that the curve SL traverses the (κ_1, κ_2) -plane several times close to the line $\kappa_1 + \kappa_2 = \gamma(a_2/a_1 - 2) \approx 12.4$ where the singular fold bifurcation L_{00} occurs in the $\varepsilon \rightarrow 0$ singular limit of (1.3); see [33]. Moreover, SL extends to very low values of κ_2 ; in fact, in one-parameter bifurcation diagrams in κ_1 for fixed κ_2 , it generates the first observed folds in the branch of periodic orbits that bifurcate from the Hopf bifurcation H_1 as κ_2 is increased; see [34].

Figure 13 can be seen as a summary and overview of the level of complexity of the dynamics one can find in (1.3). In a sense, the overall bifurcation diagram in the (κ_1, κ_2) -plane of the two feedback strengths would not be particularly unusual for a nonlinear DDE. Its surprising aspect is, however, that all the phenomena it represents are entirely due to the state dependence. As the state-dependent parameters c_1 and c_2 of the delays are decreased to zero, the bifurcation structure in Figure 13, including the Hopf-Hopf bifurcation points and induced dynamics on tori, will disappear. Indeed, (1.3) for $c_1 = c_2 = 0$ is entirely linear and, hence, does not have any nontrivial dynamics. Hence, if one were to replace the state dependence by constant delays, none of the dynamics we reported would be found. Admittedly, (1.3) has been constructed as an extreme case in this regard. Nevertheless, the study presented here should be seen as a warning: replacing state dependence by a constant-delay approximation may result in the disappearance of the very dynamics one intends to study. This may be the case even when the approximating constant-delay DDE is actually nonlinear itself.

State-dependent DDEs have been suggested as suitable models in a number of applications [10, 36, 38, 68, 82]. We hope that the study presented here may serve as a demonstration of what can be achieved by a combination of analytical and numerical tools when it comes to the bifurcation analysis of a given state-dependent DDE. It is now possible to study models from this class effectively in their own right, and to determine the role the state dependence plays in the observed dynamics. In fact, normal form calculations and numerical continuation tools are able to produce consistent results, such as the type of codimension-two bifurcation or the existence and organization of resonances on tori, for which, as yet, the respective theory has not been developed for state-dependent DDEs. We believe that case studies of specific systems are also a useful way of guiding the further development of theory for state-dependent DDEs. At the same time, numerical methods also continue to be developed further. For example, the curves shown in Figure 13 were computed with recently implemented routines of DDE-BIFTOOL [72] that allow the continuation in two parameters of codimension-one bifurcation

of periodic orbits to determine curves of saddle-node, period-doubling, and torus bifurcations. Previously, such curves could only be constructed by detecting the respective bifurcation in one-parameter continuations, which is certainly not a suitable method for finding complicated bifurcation curves such as SL in Figure 13(b). In a nutshell, practically all advanced tools for the bifurcation analysis of DDEs are now also available when state dependence is present.

Acknowledgments. The authors are grateful for support from the American Institute for Mathematical Sciences for our participation in the workshop “Low dimensional structures in dynamical systems with variable time lags,” where this research collaboration was initiated. R.C.C. thanks the Department of Mathematics and Statistics at McGill for their hospitality during his time as a Postdoctoral Fellow and now as an Adjunct Member of the department. He is also grateful to the FQRNT for a PBEEE award. A.R.H. thanks the University of Auckland for its hospitality and support during two research visits. We all thank Jan Sieber for fruitful discussions regarding normal form calculation within DDE-BIFTOOL, Rafael de la Llave and Xiaolong He for helpful comments on quasi-periodic solutions in state-dependent DDEs, and two anonymous referees for their very constructive feedback on the initial version of the manuscript.

REFERENCES

- [1] W. G. AIELLO, H. I. FREEDMAN, AND J. WU, *Analysis of a model representing stage-structured population growth with state-dependent time delay*, SIAM J. Appl. Math., 52 (1992), pp. 855–869, <https://doi.org/10.1137/0152048>.
- [2] D. G. ARONSON, M. A. CHORY, G. R. HALL, AND R. P. MCGEHEE, *Bifurcations from an invariant circle for two-parameter families of maps of the plane: A computer-assisted study*, Commun. Math. Phys., 83 (1982), pp. 303–354, <https://doi.org/10.1007/BF01213607>.
- [3] J. BÉLAIR AND S. A. CAMPBELL, *Stability and bifurcations of equilibria in a multiple-delayed differential equation*, SIAM J. Appl. Math., 54 (1994), pp. 1402–1424, <https://doi.org/10.1137/S0036139993248853>.
- [4] A. BELLEN AND M. ZENNARO, *Numerical Methods for Delay Differential Equations*, Numerical Mathematics and Scientific Computation, Oxford Science Publications, New York, 2003.
- [5] A. BELLEN, M. ZENNARO, S. MASET, AND N. GUGLIELMI, *Recent trends in the numerical solution of retarded functional differential equations*, Acta Numer., 18 (2009), pp. 1–110, <https://doi.org/10.1017/S0962492906390010>.
- [6] R. E. BELLMAN AND K. L. COOKE, *Differential-Difference Equations*, Academic Press, New York, 1963, <http://www.rand.org/pubs/reports/R374.html>.
- [7] D. BREDÁ, O. DIEKMANN, M. GYLLENBERG, F. SCARABEL, AND R. VERMIGLIO, *Pseudospectral discretization of nonlinear delay equations: New prospects for numerical bifurcation analysis*, SIAM J. Appl. Dyn. Syst., 15 (2016), pp. 1–23, <https://doi.org/10.1137/15M1040931>.
- [8] G. BROWN, C. M. POSTLETHWAITE, AND M. SILBER, *Time-delayed feedback control of unstable periodic orbits near a subcritical Hopf bifurcation*, Phys. D, 240 (2011), pp. 859–871, <https://doi.org/10.1016/j.physd.2010.12.011>.
- [9] M. CRAIG, A. R. HUMPHRIES, AND M. C. MACKAY, *A mathematical model of granulopoiesis incorporating the negative feedback dynamics and kinetics of G-CSF/neutrophil binding and internalization*, Bull. Math. Biol., 78 (2016), pp. 2304–2357, <https://doi.org/10.1007/s11538-016-0179-8>.
- [10] J. DE LUCA, N. GUGLIELMI, A. R. HUMPHRIES, AND A. POLITI, *Electromagnetic two-body problem: Recurrent dynamics in the presence of state-dependent delay*, J. Phys. A, 43 (2010), 205103, <https://doi.org/10.1088/1751-8113/43/20/205103>.
- [11] O. DIEKMANN, M. GYLLENBERG, J. A. J. METZ, S. NAKAOKA, AND A. M. DE ROOS, *Daphnia revisited: Local stability and bifurcation theory for physiologically structured population models explained by way of an example*, J. Math. Biol., 61 (2010), pp. 277–318, <https://doi.org/10.1007/s00285-009-0299-y>.

- [12] O. DIEKMANN, S. A. VAN GILS, S. M. VERDUYN LUNEL, AND H.-O. WALTHER, *Delay Equations, Functional-, Complex-, and Nonlinear Analysis*, Appl. Math. Sci. 110, Springer-Verlag, New York, Berlin, 1995.
- [13] H. A. DIJKSTRA, *Dynamical Oceanography*, Springer-Verlag, New York, Berlin, 2008.
- [14] R. D. DRIVER, *Existence theory for a delay-differential system*, Contrib. Differential Equations, 1 (1963), pp. 317–336.
- [15] R. D. DRIVER, *Ordinary and Delay Differential Equations*, Appl. Math. Sci. 20, Springer-Verlag, New York, Berlin, 1977.
- [16] M. EICHMANN, *A Local Hopf Bifurcation Theorem for Differential Equations with State-Dependent Delays*, Ph.D. thesis, Mathematics, Universität Gießen, Germany, 2006, <http://geb.uni-giessen.de/geb/volltexte/2006/2844/>.
- [17] K. ENGELBORGH, T. LUZYANINA, AND D. ROOSE, *Numerical bifurcation analysis of delay differential equations using DDE-BIFTOOL*, ACM Trans. Math. Software, 28 (2002), pp. 1–21, <https://doi.org/10.1145/513001.513002>.
- [18] G. FAN, S. A. CAMPBELL, G. S. WOLKOWICZ, AND H. ZHU, *The bifurcation study of 1:2 resonance in a delayed system of two coupled neurons*, J. Dynam. Differential Equations, 25 (2013), pp. 193–216, <https://doi.org/10.1007/s10884-012-9279-9>.
- [19] B. FIEDLER, V. FLUNKERT, M. GEORGI, P. HÖVEL, AND E. SCHÖLL, *Refuting the odd-number limitation of time-delayed feedback control*, Phys. Rev. Lett., 98 (2007), 114101, <https://doi.org/10.1103/PhysRevLett.98.114101>.
- [20] J. FOSS, A. LONGTIN, B. MENSOUR, AND J. MILTON, *Multistability and delayed recurrent loops*, Phys. Rev. Lett., 76 (1996), pp. 708–711, <https://doi.org/10.1103/PhysRevLett.76.708>.
- [21] P. GETTO AND M. WAURICK, *A differential equation with state-dependent delay from cell population biology*, J. Differential Equations, 260 (2016), pp. 6176–6200, <https://doi.org/10.1016/j.jde.2015.12.038>.
- [22] K. GREEN, B. KRAUSKOPF, AND K. ENGELBORGH, *Bistability and torus break-up in a semiconductor laser with phase-conjugate feedback*, Phys. D, 173 (2002), pp. 114–129, [https://doi.org/10.1016/S0167-2789\(02\)00656-5](https://doi.org/10.1016/S0167-2789(02)00656-5).
- [23] S. GUO AND J. WU, *Bifurcation Theory of Functional Differential Equations*, Appl. Math. Sci. 184, Springer-Verlag, New York, 2013.
- [24] I. GYÖRI AND F. HARTUNG, *On the exponential stability of a state-dependent delay equation*, Acta Sci. Math. (Szeged), 66 (2000), pp. 71–84.
- [25] I. GYÖRI AND F. HARTUNG, *Exponential stability of a state-dependent delay system*, Discrete Contin. Dyn. Syst. Ser. A, 18 (2007), pp. 773–791, <https://doi.org/10.3934/dcds.2007.18.773>.
- [26] J. K. HALE, *Theory of Functional Differential Equations*, Appl. Math. Sci. 3, Springer-Verlag, New York, 1977.
- [27] J. K. HALE AND S. M. VERDUYN LUNEL, *Introduction to Functional-Differential Equations*, Appl. Math. Sci. 99, Springer-Verlag, New York, 1993.
- [28] F. HARTUNG, *Nonlinear variation of constants formula for differential equations with state-dependent delays*, J. Dynam. Differential Equations, 28 (2016), pp. 1187–1213, <https://doi.org/10.1007/s10884-015-9445-y>.
- [29] F. HARTUNG, T. KRISZTIN, H.-O. WALTHER, AND J. WU, *Functional differential equations with state-dependent delays: Theory and applications*, in Handbook of Differential Equations: Ordinary Differential Equations 3, A. Cañada, P. Drábek, and A. Fonda, eds., Elsevier - North-Holland, Amsterdam, 2006, pp. 435–545.
- [30] X. HE AND R. DE LA LLAVE, *Construction of quasi-periodic solutions of state-dependent delay differential equations by the parameterization method I: Finitely differentiable, hyperbolic case*, J. Dynam. Differential Equations, (2016), <https://doi.org/10.1007/s10884-016-9522-x>.
- [31] X. HE AND R. DE LA LLAVE, *Construction of quasi-periodic solutions of state-dependent delay differential equations by the parameterization method II: Analytic case*, J. Differential Equations, 261 (2016), pp. 2068–2108, <https://doi.org/10.1016/j.jde.2016.04.024>.
- [32] Q. HU AND J. WU, *Global Hopf bifurcation for differential equations with state-dependent delay*, J. Differential Equations, 248 (2010), pp. 2801–2840, <https://doi.org/10.1016/j.jde.2010.03.020>.

- [33] A. R. HUMPHRIES, D. A. BERNUCCI, R. CALLEJA, N. HOMAYOUNFAR, AND M. SNARSKI, *Periodic solutions of a singularly perturbed delay differential equation with two state-dependent delays*, J. Dynam. Differential Equations, 28 (2016), pp. 1215–1263, <https://doi.org/10.1007/s10884-015-9484-4>.
- [34] A. R. HUMPHRIES, O. A. DEMASI, F. M. G. MAGPANTAY, AND F. UPHAM, *Dynamics of a delay differential equation with multiple state-dependent delays*, Discrete Contin. Dyn. Syst. Ser. A, 32 (2012), pp. 2701–2727, <https://doi.org/10.3934/dcds.2012.32.2701>.
- [35] T. INSPERGER, J. MILTON, AND G. STÉPÁN, *Acceleration feedback improves balancing against reflex delay*, J. Roy. Soc. Interface, 10 (2012), 79, <https://doi.org/10.1098/rsif.2012.0763>.
- [36] T. INSPERGER, G. STÉPÁN, AND J. TURI, *State-dependent delay in regenerative turning processes*, Nonlinear Dyn., 47 (2007), pp. 275–283, <https://doi.org/10.1007/s11071-006-9068-2>.
- [37] S. G. JANSSENS, *On a normalization technique for codimension two bifurcations of equilibria of delay differential equations*, Master's thesis, Faculty of Science, Universiteit Utrecht, The Netherlands, 2010, dspace.library.uu.nl/handle/1874/312252.
- [38] R. JESSOP AND S. A. CAMPBELL, *Approximating the stability region of a neural network with a general distribution of delays*, Neural Netw., 23 (2010), pp. 1187–1201, <https://doi.org/10.1016/j.neunet.2010.06.009>.
- [39] W. JUST, B. FIEDLER, M. GEORGI, V. FLUNKERT, P. HÖVEL, AND E. SCHÖLL, *Beyond the odd number limitation: A bifurcation analysis of time-delayed feedback control*, Phys. Rev. E, 76 (2007), 026210, <https://doi.org/10.1103/PhysRevE.76.026210>.
- [40] D. M. KANE AND K. A. SHORE, EDS., *Unlocking Dynamical Diversity: Optical Feedback Effects on Semiconductor Lasers*, Wiley, New York, 2005.
- [41] H. KAPER AND H. ENGLER, *Mathematics and Climate*, SIAM, Philadelphia, 2013.
- [42] M. KLOOSTERMAN, S. A. CAMPBELL, AND F. J. POULIN, *A closed NPZ model with delayed nutrient recycling*, J. Math. Biol., 68 (2014), pp. 815–850, <https://doi.org/10.1007/s00285-013-0646-x>.
- [43] G. KOZYREFF AND T. ERNEUX, *Singular Hopf bifurcation in a differential equation with large state-dependent delay*, Proc. R. Soc. A, 470 (2013), 0596, <https://doi.org/10.1098/rspa.2013.0596>.
- [44] B. KRAUSKOPF, *Bifurcation sequences at 1:4 resonance: An inventory*, Nonlinearity, 7 (1994), pp. 1073–1091, <https://doi.org/10.1088/0951-7715/7/3/017>.
- [45] B. KRAUSKOPF, *The bifurcation set for the 1:4 resonance problem*, Exper. Math., 3 (1994), pp. 107–128, <https://doi.org/10.1080/10586458.1994.10504283>.
- [46] B. KRAUSKOPF AND D. D. LENSTRA, EDS., *Fundamental Issues of Nonlinear Laser Dynamics*, AIP Conf. Proc. 548, American Institute of Physics, College Park, MD, 2000.
- [47] B. KRAUSKOPF AND K. GREEN, *Computing unstable manifolds of periodic orbits in delay differential equations*, J. Comput. Math., 186 (2003), pp. 230–249, [https://doi.org/10.1016/S0021-9991\(03\)00050-0](https://doi.org/10.1016/S0021-9991(03)00050-0).
- [48] B. KRAUSKOPF AND J. SIEBER, *Bifurcation analysis of delay-induced resonances of the El-Niño southern oscillation*, Proc. R. Soc. A, 470 (2014), 2169, <https://doi.org/10.1098/rspa.2014.0348>.
- [49] T. KRISZTIN, *A local unstable manifold for differential equations with state-dependent delay*, Discrete Contin. Dyn. Syst. Ser. A, 9 (2003), pp. 993–1028, <https://doi.org/10.3934/dcds.2003.9.993>.
- [50] T. KRISZTIN, *C^1 -smoothness of center manifolds for differential equations with state-dependent delay*, in Nonlinear Dynamics and Evolution Equations, X.-Q. Z. Hermann Brunner and X. Zou, eds., Fields Inst. Commun. 48, Amer. Math. Soc., Providence, RI, 2006, pp. 213–226.
- [51] Y. A. KUZNETSOV, *Elements of Applied Bifurcation Theory*, 3rd ed., Appl. Math. Sci. 112, Springer-Verlag, New York, 2004.
- [52] Y. N. KYRYCHKO, K. B. BLYUSS, AND E. SCHÖLL, *Amplitude and phase dynamics in oscillators with distributed-delay coupling*, Phil. Trans. R. Soc. A, 371 (2013), <https://doi.org/10.1098/rsta.2012.0466>.
- [53] V. G. LEBLANC, *Realizability of the normal form for the triple-zero nilpotency in a class of delayed nonlinear oscillators*, J. Differential Equations, 254 (2013), pp. 637–647, <https://doi.org/10.1016/j.jde.2012.09.008>.
- [54] K. LÜDGE, ED., *Nonlinear Laser Dynamics. From Quantum Dots to Cryptography*, Wiley-VCH, New York, 2012.
- [55] M. C. MACKAY AND L. GLASS, *Oscillation and chaos in physiological control systems*, Science, 197 (1977), pp. 287–289, <https://doi.org/10.1126/science.267326>.
- [56] J. MALLET-PARET AND R. D. NUSSBAUM, *Boundary layer phenomena for differential-delay equations with state-dependent time lags*, I. Arch. Ration. Mech. Anal., 120 (1992), pp. 99–146, <https://doi.org/10.1007/BF00418497>.

- [57] J. MALLET-PARET AND R. D. NUSSBAUM, *Boundary layer phenomena for differential-delay equations with state-dependent time lags: II*, J. Reine Angew. Math., 477 (1996), pp. 129–197.
- [58] J. MALLET-PARET AND R. D. NUSSBAUM, *Boundary layer phenomena for differential-delay equations with state-dependent time lags: III*, J. Differential Equations, 189 (2003), pp. 640–692, [https://doi.org/10.1016/S0022-0396\(02\)00088-8](https://doi.org/10.1016/S0022-0396(02)00088-8).
- [59] J. MALLET-PARET AND R. D. NUSSBAUM, *Stability of periodic solutions of state-dependent delay-differential equations*, J. Differential Equations, 250 (2011), pp. 4085–4103, <https://doi.org/10.1016/j.jde.2010.10.023>.
- [60] J. MALLET-PARET AND R. D. NUSSBAUM, *Superstability and rigorous asymptotics in singularly perturbed state-dependent delay-differential equations*, J. Differential Equations, 250 (2011), pp. 4037–4084, <https://doi.org/10.1016/j.jde.2010.10.024>.
- [61] J. MALLET-PARET AND R. D. NUSSBAUM, *Periodic Solutions of Differential Equations with Two State-Dependent Delays*, (2017), in preparation.
- [62] J. MALLET-PARET, R. D. NUSSBAUM, AND P. PARASKEVOPOULOS, *Periodic solutions for functional differential equations with multiple state-dependent time lags*, Topol. Methods Nonlinear Anal., 3 (1994), pp. 101–162.
- [63] MATHWORKS, *MATLAB 2015b*, Mathworks, Natick, MA, 2015.
- [64] J. MILTON, J. L. TOWNSEND, M. A. KING, AND T. OHIRA, *Balancing with positive feedback: The case for discontinuous control*, Phil. Trans. R. Soc. A, 367 (2009), pp. 1181–1193, <https://doi.org/10.1098/rsta.2008.0257>.
- [65] C. M. POSTLETHWAITE, *Stabilization of long-period periodic orbits using time-delayed feedback control*, SIAM J. Appl. Dyn. Syst., 8 (2009), pp. 21–39, <https://doi.org/10.1137/080721510>.
- [66] A. S. PUREWAL, C. M. POSTLETHWAITE, AND B. KRAUSKOPF, *A global bifurcation analysis of the subcritical Hopf normal form subject to Pyragas time-delayed feedback control*, SIAM J. Appl. Dyn. Syst., 13 (2014), pp. 1879–1915, <https://doi.org/10.1137/130949804>.
- [67] K. PYRAGAS, *Continuous control of chaos by self-controlling feedback*, Phys. Lett. A, 170 (1992), pp. 421–428, [https://doi.org/10.1016/0375-9601\(92\)90745-8](https://doi.org/10.1016/0375-9601(92)90745-8).
- [68] V. PYRAGAS AND K. PYRAGAS, *Adaptive modification of the delayed feedback control algorithm with a continuously varying time delay*, Phys. Lett. A, 375 (2011), pp. 3866–3871, <https://doi.org/10.1016/j.physleta.2011.08.072>.
- [69] R. QESMI AND H.-O. WALTHER, *Center-stable manifolds for differential equations with state-dependent delays*, Discrete Contin. Dyn. Syst. Ser. A, 23 (2009), pp. 1009–1033, <https://doi.org/10.3934/dcds.2009.23.1009>.
- [70] E. SCHÖLL, G. HILLER, P. HÖVEL, AND M. A. DAHLEM, *Time-delayed feedback in neurosystems*, Phil. Trans. R. Soc. A, 367 (2009), pp. 1079–1096, <https://doi.org/10.1098/rsta.2008.0258>.
- [71] J. SIEBER, *Finding periodic orbits in state-dependent delay differential equations as roots of algebraic equations*, Discrete Contin. Dyn. Syst. Ser. A, 32 (2012), pp. 2607–2651, <https://doi.org/10.3934/dcds.2012.32.2607>.
- [72] J. SIEBER, K. ENGELBORGHES, T. LUZYANINA, G. SAMAËY, AND D. ROOSE, *DDE-BIFTOOL Manual—Bifurcation analysis of delay differential equations*, 2015, <https://arxiv.org/abs/1406.7144>.
- [73] R. SIPAHI, F. M. ATAY, AND S.-I. NICULESCU, *Stability of traffic flow behavior with distributed delays modeling the memory effects of the drivers*, SIAM J. Appl. Math., 68 (2007), pp. 738–759, <https://doi.org/10.1137/060673813>.
- [74] H. SMITH, *An Introduction to Delay Differential Equations with Applications to the Life Sciences*, Texts in Appl. Math., Springer, New York, 2011.
- [75] G. STÉPÁN, *Retarded dynamical systems: Stability and characteristic functions*, Longman Scientific & Technical, Harlow, UK, 1989.
- [76] E. STUMPF, *On a differential equation with state-dependent delay: A center-unstable manifold connecting an equilibrium and a periodic orbit*, J. Dynam. Differential Equations, 24 (2012), pp. 197–248, <https://doi.org/10.1007/s10884-012-9245-6>.
- [77] R. SZALAI AND D. ROOSE, *Continuation and bifurcation analysis of delay differential equations*, in Numerical Continuation Methods for Dynamical Systems: Path Following and Boundary Value Problems, B. Krauskopf, H. M. Osinga, and J. Galán-Vioque, eds., Springer-Verlag, New York, Berlin, 2007, pp. 359–399.

- [78] B. I. WAGE, *Normal Form Computations for Delay Differential Equations in DDE-BIFTOOL*, Master's thesis, Faculty of Science, Universiteit Utrecht, The Netherlands, 2014, dspace.library.uu.nl/handle/1874/296912.
- [79] E. WALL, F. GUICHARD, AND A. R. HUMPHRIES, *Synchronization in ecological systems by weak dispersal coupling with time delay*, *Theor. Ecol.*, 6 (2013), pp. 405–418, <https://doi.org/10.1007/s12080-013-0176-6>.
- [80] H.-O. WALTHER, *Smoothness properties of semiflows for differential equations with state-dependent delays*, *J. Math. Sci.*, 124 (2004), pp. 5193–5207, <https://doi.org/doi:10.1023/B:JOTH.0000047253.23098.12>.
- [81] H.-O. WALTHER, *Complicated histories close to a homoclinic loop generated by variable delay*, *Adv. Differential Equations*, 19 (2014), pp. 911–946, <http://projecteuclid.org/euclid.ade/1404230128>.
- [82] Y. YUAN AND J. BÉLAIR, *Threshold dynamics in an SEIRS model with latency and temporary immunity*, *J. Math. Biol.*, 69 (2014), pp. 875–904, <https://doi.org/10.1007/s00285-013-0720-4>.